Theses, Dissertations and Capstones

1-1-2006

# Spectroscopic and Thermodynamic Analysis of CO Rebinding and Photodissociation from Fe (II) LPO

Dustin Michael Lockney

Follow this and additional works at: http://mds.marshall.edu/etd

Part of the Physical Chemistry Commons

Spectroscopic and Thermodynamic Analysis of

CO Rebinding and Photodissociation from $Fe^{(II)}LPO$

Thesis submitted to
the Graduate College of
Marshall University

In partial fulfillment of
the requirements for the degree of
Master of Science
in Chemistry

by

Dustin Michael Lockney

Dr. Jaroslava Miksovska, Ph.D., Committee Chairperson
Dr. William Price, Ph.D.
Dr. Leslie Frost, Ph.D.

Marshall University

May, 2006

# Abstract

Spectroscopic and Thermodynamic Analysis of

CO Rebinding and Photodissociation from $Fe^{(II)}LPO$

By Dustin Michael Lockney

Lactoperoxidase (LPO) is a heme peroxidase found in tears, milk, saliva, and cervical fluids that has bactericidal activity. The bactericidal nature of LPO is due to its ability to oxidize halides and pseudohalides in the presence of $H_2O_2$. Full understanding of the catalytic cycle of LPO requires detailed characterization of the mechanism of ligand binding to the enzyme active site. This includes a dynamic and energetic description of conformational changes associated with heme-ligand interactions. Photoacoustic calorimetry is applied to determine the kinetics and magnitude of reaction volume and enthalpy changes for CO dissociation from CO-LPO. Time-resolved absorption spectroscopy was used to determine activation enthalpy and entropy of photodissociation of CO from CO-LPO as well. UV-visible spectroscopy indicated that, upon reduction of LPO with sodium dithionite, an intermediate state ($Fe^{(II)}LPO_{intermediate}$) forms, that biphasically relaxes to a final reduced state ($Fe^{(II)}LPO_{final}$). We show that the rate constant for conversion of $Fe^{(II)}LPO_{intermediate}$ to $Fe^{(II)}LPO_{final}$ is pH dependant and propose that $Fe^{(II)}LPO_{intermediate}$ exists in two conformations. The conformation at neutral pH exhibits a fast conversion, whereas at high pH the conformation with slow conversion is populated. We speculate that the protonation state of Arg372, that is located in the heme-binding pocket, may control the conversion rate. Transient absorption spectroscopy results show that CO rebinding to $Fe^{(II)}LPO$, is pH dependant, with CO rebinding faster at higher pH. At pH=4.0 and 7.0, the rate constant of recombination of

CO to LPO is $2.7 \times 10^4$ $M^{-1} \cdot s^{-1}$ and $4.9 \times 10^4$ $M^{-1} \cdot s^{-1}$, respectively. In 100 mM CAPS buffer (pH=10.0) recombination is biphasic with the fast rate constant $8.4 \times 10^4$ $M^{-1} \cdot s^{-1}$ and the slow rate constant $1.3 \times 10^4$ $M^{-1} \cdot s^{-1}$. Photoacoustic calorimetry results show that photodissociation of CO from $Fe^{(II)}LPO$ is exothermic at neutral pH ($\Delta H$=-16.3$\pm$4.6kcal·mol$^{-1}$) and acidic pH ($\Delta H$=-12.5 $\pm$ 5.5kcal·mol$^{-1}$), with volume change of ~3ml·mol$^{-1}$. Photolysis of CO-Fe at pH=10.0 and in 500 mM NaCl buffers (pH=7.0) is an endothermic process with a change in volume of ~3 ml·mol$^{-1}$. The small volume changes observed suggest that, in addition to photolysis of the CO-Fe bond and solvation of the CO molecule, other processes contribute to the observed volume and enthalpy changes. It is likely that dissociation of CO is associated with breakage of a salt bridge between Arg557 and the ring-D propionate group. Changes in the protein charge distribution are likely to cause electrostriction and therefore results in the smaller volume change. This is confirmed by the fact that, at pH=10.0 and 500 mM NaCl buffer (pH=7.0), the observed enthalpy change corresponds to the enthalpy of the CO-Fe bond whereas the enthalpy change is exothermic at pH=4.0 and 7.0.

**Acknowledgements**

I would like to give special thanks to my research advisor, Jarka, for all her help, hard work and motivation on this project. My success and future success would not have been possible without her.

Special thanks to my family for their support and guidance. I would like to acknowledge my research group for their support as well.

I would also like to thank the chemistry department at Marshall University for their advice and mentoring along the way.

**List of Figures**

## List of Tables

# List of Abbreviations

Carboxylactoperoxidase (CO-LPO)

Eosinophil peroxidase (EPO)

$Fe^{(III)}$meso-tetra(4-sulfonatophenyl)porphyrin chloride (4sp)

Horseradish peroxidase (HRP)

Lactoperoxidase (LPO)

Myeloperoxidase (MPO)

Myoglobin (Mb)

Oxidized lactoperoxidase ($Fe^{(III)}$LPO)

Photoacoustic calorimetry (PAC)

Porphyrin (Por)

Protoporphyrin IX (PPIX)

Reduced lactoperoxidase ($Fe^{(II)}$LPO)

Thyroid peroxidase (TPO)

Transient absorption spectroscopy (TA)

# 1.0 Introduction

## 1.1 Heme peroxidases

Proteins perform many physiological functions [1]. One of their fundamental responsibilities is to act as an enzyme catalyst. Enzymatic proteins fit into six classes of enzymes: oxidoreductases, transferases, hydrolyases, lyases, isomerases, and ligases. The functionality of a third of these proteins is dependent on metal cofactors, that are crucial to their enzymatic activity [1]. Metal cofactors are structures in an enzyme that incorporate transition metals; the empty d-orbitals act as electron acceptors and donors [1]. A common metal cofactor found in oxygen binding, transporting and sensing proteins and in oxidoreductases is iron-protoporphyrin IX (PPIX). Ferriprotoporphyrin IX is a tetrapyrrole ring with a $Fe^{(III)}$ coordinated to the center of the ring; ferroprotoporphyrin IX has a $Fe^{(II)}$ coordinated to the center [2]. The tetrapyrrole ring has eight side chains (four methyl groups, two vinyl groups, and two propionate groups). The structure of protoporphyrin IX is shown in Figure 1.1 [2]. PPIX is attached to the protein moiety through axial coordination with the imidazole group of a histidine residue, and through ionic interactions between the propionic groups and positively charged residues, such as lysine and arginine, as well as hydrophobic interactions.
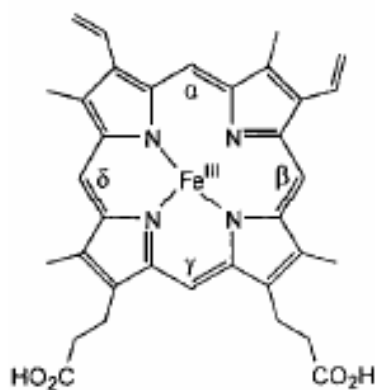


Figure 1.1 Structure of iron-protoporphyrin IX [3]. PPIX has an iron coordinated to the center of a tetrapyrrole ring and eight side chains (four methyl groups, two vinyl groups, and two propionate groups).

The natural coordination chemistry for Fe is a 3+ oxidation state with six monodentate ligands. However, oxygen-carrying proteins, for example hemoglobin, have a five-coordinate, high-spin, $Fe^{(II)}$ heme. Several studies have shown that the hydrophobic pocket of the protein maintains the reduced state of the heme. Heme oxygenases are the only known enzyme to be able to degrade heme in mammals [3]. The enzyme oxidizes the α-methene of the tetrapyrrole ring, forming $Fe^{(II)}$ and bilirubin [3]. Another interesting group of heme proteins is represented by oxygen sensing proteins like FixL and EcDos. These sensors have the ability to sense $O_2$ and distinguish $O_2$ from other small molecules like CO and NO [4]. Oxygen binding to the heme domain of these sensors results in a decrease in phosphorylation activity of their kinase domain. This ultimately leads to inhibition of nitrogen fixation genes [4]. The diversity of the enzymatic activity of these proteins, in spite of their similar heme moiety, is attributed to the protein environment, different functional groups on the tetrapyrrole ring, different axial ligands, and the higher order structure of the protein and protein complexes [4].

Among heme proteins, heme peroxidases are of particular interest due to their unique ability to oxidize halides (HX) and pseudohalides ($SCN^-$) in the presence of hydrogen peroxide, to form hypohalides and free radicals ($X^{\cdot}$, HOX, HOSCN or $SCN^{\cdot}$). The hypohalides and free radicals are believed to participate in the antimicrobial defense system [5]. Peroxidases are split into two superfamilies, plant and mammalian. The major difference between the two superfamilies is that the heme is covalently bound to the protein in the mammalian superfamily and the covalent attachment is absent in the plant superfamily [6]. The plant superfamily is organized into three classes. Class I are the intracellular peroxidases. Class II and III are fungal and plant peroxidases,

respectively. Horseradish peroxidase (HRP) is the most studied plant peroxidase. The physiological substrates of HRP are small aromatic molecules (plant hormones, which are similar to the organic substrates of lactoperoxidase (LPO), eosinophil peroxidase (EPO), and myeloperoxidase (MPO)). HRP is thought to aid in cell wall maintenance by protecting against peroxidative damage, and participates in synthesis and degradation of lignin [8].

Some of the first peroxidases discovered were in mammals but since then other peroxidases have been discovered in mollusks and have similar structure and activity as to that of mammalian peroxidases [2]. The mammalian superfamily in this case is referred to as the animal peroxidase superfamily. Some of the most studied peroxidases of the mammalian superfamily are LPO, MPO, EPO, and thyroid peroxidase (TPO). LPO, EPO, and MPO are coded from human chromosome 17 and the genes for LPO and MPO are laid out tail-to-tail and have similar introns and exons (the two genes spanning 90kbp) [7]. The promoter regions have not yet been identified. These enzymes participate in the body's antimicrobial defense system.

## 1.2    Biological relevance of lactoperoxidase

LPO is secreted into areas that are open and prone to infection, and therefore is found in exocrine secretions such as saliva, sweat, tears, milk, and cervical fluid [9]. LPO acts as part of the body's first line of defense against microbes, bacteria and viruses [10]. The importance of LPO in anti-microbial activities is several. In infants, born without an established immune system, LPO provides defense against infection in the intestines. It has been shown that infants have an increased level of LPO and thiocyanate in their saliva [11, 12]. During the rest of a human life cycle there does not seem to be an

elevation in levels of LPO, except in older adults to fight off gingivitis, and in women during menstruation and pregnancy. The correlation between the high levels of LPO and menstruation and pregnancy are directly related to increased levels of estrogen [13]. In other studies LPO has been shown to irreversibly bind to tooth enamel in an active form. Research in the use of LPO to prevent cavities is also being explored [13].

LPO that has been secreted from mammary glands is speculated to be a risk factor for breast cancer. Highly hydrophobic molecules that are not physiological substrates of LPO (such as aromatic amines) are accumulated through diet. These tend to migrate to areas of the body with higher levels of adipose tissue [14]. In the presence of hydrogen peroxide, LPO may catalyze the oxidation of such organic molecules and during reaction free radicals with mutagenic capabilities are released [14, 15]. On the other hand, research has also shown that LPO and other peroxidases possess the ability to deactivate certain carcinogens *in vitro* [16].

## 1.3 Structure of lactoperoxidase

### 1.3.1 Apoprotein

Several different methods for isolation and extraction of LPO have been shown to produce different fractions of proteins [11, 17, 18]. Through sequencing and analysis of chemical composition and enzymatic activity, the variations in molecular weight of the different fractions of LPO are attributed to different glyclosylation states and possible deamidation (depending on the technique of isolation) of arginine residues [11, 18]. Genetic contributions to the different fractions of LPO were discarded based on studies of single animals [11, 18]. The presence of carbohydrate is thought to allow the protein to be adsorbed to bacterial and viral surfaces.

The primary structure of LPO is a 612-residue monomer and its molecular weight is approximately 80 kDa. Carbohydrates contribute approximately 10% of the total mass [20]. The tertiary structure of LPO is unknown due to the inability to crystallize LPO; therefore, there is no X-ray crystal structure available. Based on the high sequence homology and similar enzymatic activity of LPO and MPO [19], De Gioia *et al* [9] have built a 3-dimensional model of LPO on the scaffold of the X-ray crystal structure of MPO [9]. From the model of LPO it was determined that there are 4 to 5 N-glyclosylation sites, located at positions 6, 9, 112, 222, and 258 [20]. The apoprotein of LPO is highly α-helical, like most heme proteins, and is stabilized by eight disulfide bonds [19]. In addition, the enzyme is stabilized by the presence of a calcium ion. Asp227 is likely to be a key residue in the Ca$^{(II)}$ binding site. Its mutation to Ala prevents Ca$^{(II)}$ from binding and causes LPO to precipitate [21]. The model of LPO is show in Figure 1.2.
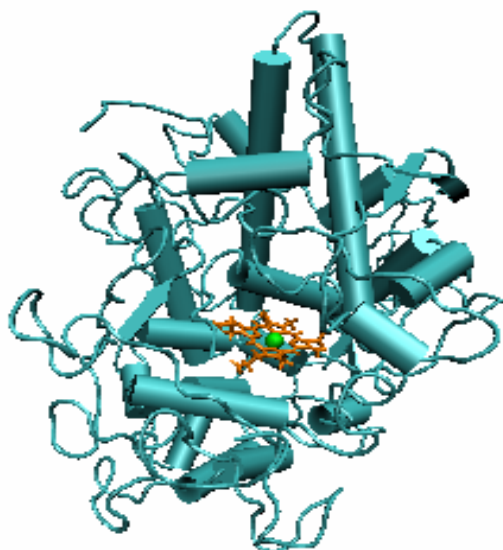


Figure 1.2: Cartoon structure of LPO. The structure was modeled using coordinates published by De Gioia et al [9], and visualized with VMD 1.8.2.

### 1.3.2   Active site

From the 3-D model of LPO, it has been proposed that several ionic residues are located in the distal pocket, including Arg372, His226, Glu375, and Asp225.   These residues are thought to participate in the enzymatic activity of LPO. Access to the active site is through a hydrophobic channel composed of phenylalanine residues (230, 277, 278, 356, 371, 498, 539, and 548).   This is reflected by LPO's high affinity for hydrophobic substrates.   On the other hand, the surface of the protein, near the access channel, has polar and charged residues: Gln245, Glu233, Glu247, Glu248, and Tyr249 [9]. These residues are thought to play a role in substrate recognition [9]. The hydrophobic access channel to the distal heme pocket is shown in Figure 1.3. Resonance Raman analysis and stopped flow studies of the active site indicate a narrow or constrained distal heme pocket, compared to that of hemoglobin and myoglobin [23, 24]. Substrate access is gated by two highly conserved residues, Arg372 ($pK_a$=9.53) and His226 ($pK_a$=5.41), located in the distal heme binding site [24, 26].

The heme in LPO, at room temperature, is a high-spin, six-coordinate, bis(hydroxymethyl) derivative of protoporphyrin IX, shown in Figure 1.4 [25]. The 1- and 5-methyl groups are covalently linked to Asp225 and Glu375 of the protein through ester bonds [26]. The ester bonds to the apoprotein are thought to function as electron withdrawing groups and also provide steric protection to its 2,4-vinyl functional groups [27].  For example, in the presence of $H_2O_2$ and SCN⁻, both LPO and HRP will generate HOSCN.  HOSCN is an electrophilic species that will then react with the vinyl groups on the heme of horseradish peroxidase [28].  This reaction does not occur with LPO. The

structure of the active site of LPO is shown in Figure 1.5.  The Fe is proximally ligated to

His468 and loosely bound to a water molecule in the distal heme pocket.
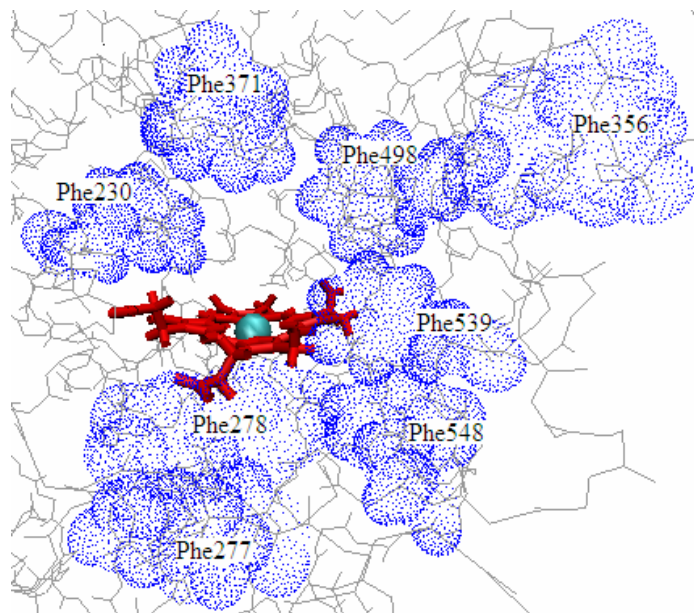


Figure 1.3: View of access channel and active site of LPO. The phenylalanine residues forming the hydrophobic access channel are shown as dotted clouds. Image was made using the De Gioia *et al* coordinates [9] and VMD 1.8.
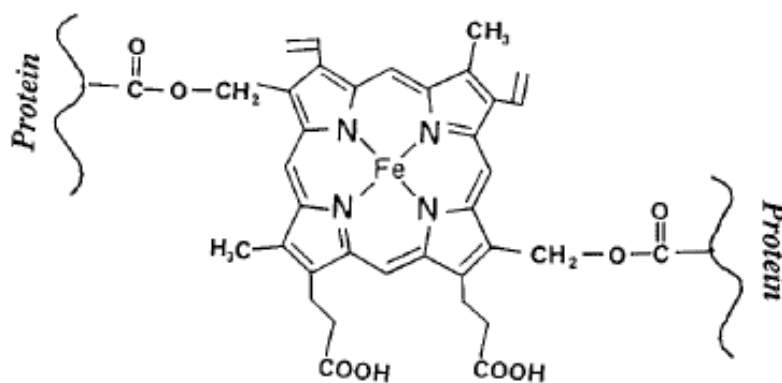


Figure 1.4: Protoporphyrin IX derivative found in LPO. The 1- and 5-methyl groups are covalently bound to the apoprotein through ester bounds to Asp225 and Glu375, respectively [23].
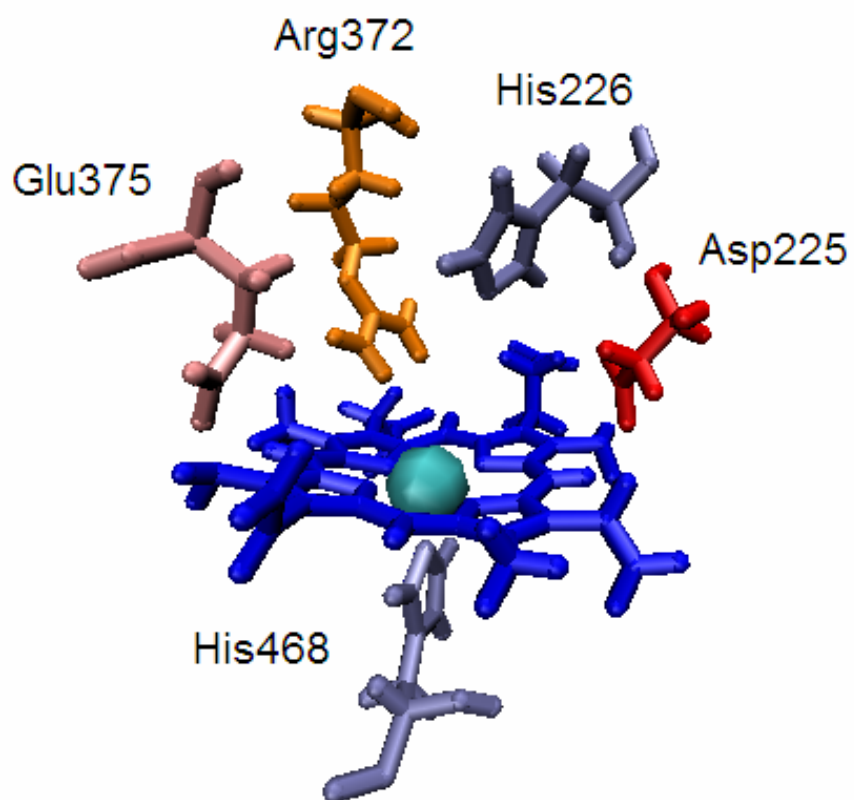
Figure 1.5: Active site of LPO. The image was made using the VMD 1.8 and the coordinates published by De Gioia *et al* [9]. Ester bonds between Glu375 and Asp225 are not shown.

## 1.4 Catalytic cycle of lactoperoxidase

LPO possesses a complex catalytic pathway, allowing it to have both peroxidase activity and catalase-like activity [29]. The peroxidase activity allows LPO to oxidize halides (Br$^-$ and I$^-$), pseudohalides (SCN$^-$), and organic molecules (phenols, catecholamines, and catechols) in the presence of $H_2O_2$ [30]. The catalase-like activity, which is not the primary activity, converts $H_2O_2$ to $O_2$ and $H_2O$ in the stoichiometric ratio 2:1:2.

During the catalytic cycle $Fe^{(III)}$ LPO, in the presence of equimolar amounts of $H_2O_2$, is converted to compound I and $H_2O$, Step 1 in the reaction mechanism in Figure 1.6. Compound I (aa$^{+\bullet}$PorFe$^{(IV)}$=O) is an oxferryl compound with a porphyrin π-cation radical (Por$^{+\bullet}$) [31, 32]. Figure 1.7 shows the detailed reaction scheme for compound I formation in LPO [33]. At physiological pH, one of the O atoms of hydrogen peroxide binds to the $Fe^{(III)}$ heme and forms a hydrogen bond to the $N_\varepsilon$ of the imidazole group from His226, intermediate A. His226 then transfers the proton and electron pair to the hydroxyl group distal to the bound oxygen atom, the step from intermediate B to C. The O-O bond is then heterolytically cleaved to form Compound I and an $H_2O$ molecule, intermediate D.

From this point there are two mechanistic pathways for LPO compound I shown in Figure 1.6. The reduction potential, 1.09 V [6], of LPO compound I, allows LPO to bielectronically oxidize SCN$^-$ to HOSCN and regenerate the ferric resting state enzyme (Step 2) in Figure 1.6. LPO can also monoelectronically oxidize halides or pseudohalides to form compound II [31] (Step 3) in Figure 1.6. In the peroxidase mechanism, compound II, in the presence of superoxide or an additional substrate (halide or pseudo-

halide) will form $O_2$ or the radical halide or radical pseudohalide species, respectively. This restores LPO back to its ferric resting state, shown in Step 4 [32,33,34].

The catalase activity, which only occurs with a 50-fold excess of hydrogen peroxide, is not the primary catalytic activity of LPO [30]. The catalase mechanism is dependent on excess of $H_2O_2$ to stabilize compound II in order to form compound III [34]. In the absence of a suitable substrate, compound I will convert to an isoelectronic species, with the radical located on the protein (aa) (step 5) [32]. The residue on which the radical is located is not known at this time. The isoelectronic form of compound I will convert to a stable form (Step 6), losing an oxidizing equivalent, and having similar characteristics as that of compound II [6]. Compound II will then react with $H_2O_2$ to form Compound III (Step 7). Compound III is composed of a superoxide molecule coordinated to $Fe^{(III)}$LPO. Step 8 shows the release of superoxide regenerating $Fe^{(III)}$LPO. This is the so-called catalase-like activity [28]. The oxygen release from compound III is the rate-limiting step in the catalase activity. The catalase activity of LPO is thought to be a mechanism to protect cells against peroxidative cell damage [30].
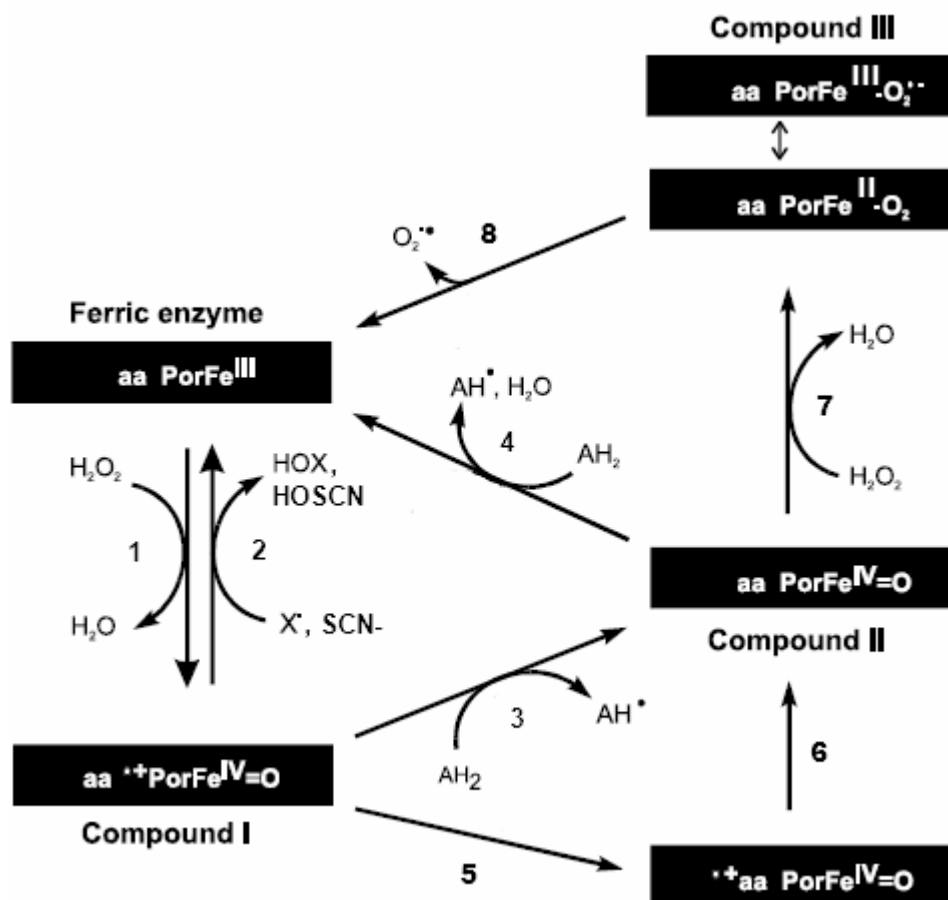
Figure 1.6: The peroxidase and catalase mechanism of LPO. Step one shows the reaction of Ferric LPO with $H_2O_2$ to form Compound I. Compound I has a $Fe^{(IV)}$ center and an oxidizing equivalent on the porphyrin ring (Por). In the presence of a suitable substrate Compound I can bielectronically oxidize a halide or thiocyanate to form a hypohalous acid or hypothiocyante and regenerate the resting ferric enzyme, shown in step two. Compound I can also monoelectronically oxidize halides or pseudohalides forming compound II and a free radical, reaction three. Compound II has a $Fe^{(IV)}$ center with an O atom coordinated to it and has lost an oxidizing equivalent from the porphyrin ring. In the absence of a suitable substrate Compound I converts to an isoelectronic form with the porphyrin-oxidizing equivalent on an amino acid (aa), step five. The isoelectronic form of compound I will decay (losing the $^+$aa oxidizing equivalent) to a form similar to compound II, step six. Compound II, in the peroxidase mechanism, monoelectronically oxidizes an additional halide or pseudohalide (step four) to regenerate the resting ferric enzyme. In the presence of excess $H_2O_2$ compound II will react to form compound III and $H_2O$ (step seven). Compound III has a superoxide molecule coordinated to the $Fe^{(III)}$ –heme. The resting enzyme is then regenerated by release of superoxide, step eight [6].
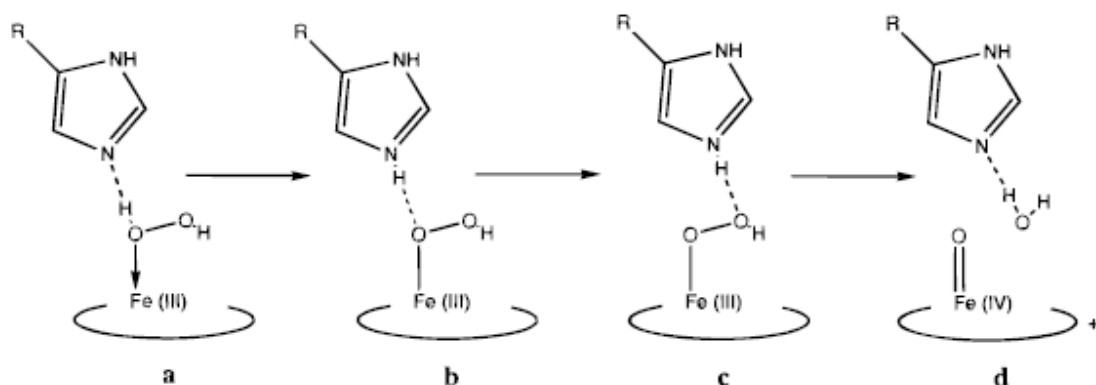


Figure 1.7: Reaction mechanism for compound I formation during the catalytic cycle. The resting enzyme with a ferric heme reacts with $H_2O_2$ to form compound I. Compound I has a heme with a $Fe^{(IV)}=O$ and a porphyrin $\pi$-cation radical [33].

## 1.5    Ligand probes

Information on how the protein structure affects the enzymatic activity of LPO is important to obtain.  To gain indirect evidence on the structure-function relationship of LPO, ligand probes in combination with spectroscopic methods become a useful tool.  In the case of LPO, ligand probes such as CO, NO, CN-, and $O_2$ are similar in size to $H_2O_2$. The additional benefit of ligand probes allows reactions to be triggered on a sub-nanosecond time scale so that information on fast processes can be obtained [24, 34, 35].

## 1.6    Objectives

The use of spectroscopic methods, in combination with ligand probes can provide information on the nature of the active site of LPO.  Although the information is important and can provide insight into the catalytic mechanism of a protein, these spectroscopic methods cannot provide information on global conformational changes associated with the catalytic cycle.

Several steps of the catalytic cycle may be controlled by changes in the protein structure, remote to the active site.  In fact, previous studies on ligand binding to hemoglobin and myoglobin have shown that ligand access to the active site is modulated by global conformational changes resulting in "gated" ligand access.

In order to study such global changes, it is beneficial to employ photothermal methods [36,37].  Photothermal methods are a group of very sensitive techniques that can be used to determine thermodynamic parameters of chemical systems on a fast time-scale (nanosecond/millisecond). Characterization of the thermodynamic parameters (molar changes in volume and enthalpy), provide insight into the mechanism of the catalytic cycle and the structure-function relationship in LPO.

Taking into account that $H_2O_2$ binding to the heme triggers the catalytic cycle, a complete understanding of the catalytic mechanism of heme peroxidases requires the characterization of the thermodynamic parameters for substrate binding to the active site. CO will be used as a ligand probe in conjunction with UV-visible spectroscopy, transient absorption spectroscopy, and photoacoustic calorimetry to investigate heme-ligand interactions and create a thermodynamic profile for CO binding to LPO. The full dynamic and energetic understanding of CO binding to LPO may contribute to our understanding of processes that occur during ligand binding and substrate selectivity.

## 2.0    Materials and Methods

## 2.1    Protein Purification and Sample Preparation:

### 2.1.1    UV-Visible spectroscopy

Native bovine lactoperoxidase (LPO) was purchased from both Sigma-Aldrich and Worthington. The name and origin of other chemicals are provided in Appendix A. UV-visible steady state absorption spectra were used to monitor protein purity and sample preparation. The spectra were recorded using a Varian UV-visible single beam spectrophotometer (Cary 50). The concentration of LPO was determined using $\varepsilon_{412} =$ 112,000 M$^{-1}$ cm$^{-1}$ [38] and the level of purity of LPO was evaluated from the RZ value (RZ=A$_{412}$/A$_{280}$). The RZ value is the absorbance of the Soret maximum (412 nm) divided by the absorbance of the protein (280 nm) [38].

### 2.1.2    Chromatography

Enzyme with an RZ value less than 0.8 was further purified using affinity liquid chromatography. Carboxymethyl cellulose (CM-52), purchased from Whatman, was prepared in a 10 0mM sodium phosphate buffer (pH=7.0). 24 ml of the cation exchange matrix, was swelled in 100 mM sodium phosphate buffer (pH=7.0), and was packed into a column. The column was then washed with 100 ml of 10 mM sodium phosphate buffer (pH=6.8). Fresh, lyophilized LPO, purchased from Sigma-Aldrich was solubilized in 10 mM sodium phosphate buffer (pH=6.8) and then loaded onto the column. The protein was then eluted with a linear ionic concentration gradient from 100 mM NaCl to 200 mM NaCl in a 10 mM sodium phosphate buffer (pH=6.8). The flow rate of 5 ml/min was controlled using a BioRad peristaltic pump. The eluate was collected in 5 ml increments

with a BioRad fraction collector. Fractions with an RZ value greater than 0.8 were pooled and concentrated by centrifugation.

### 2.1.3   Electrophoresis

Further determination of the purity of LPO from Sigma-Aldrich and Worthington was accomplished with SDS-PAGE electrophoresis.  For this procedure 7.5% and 10.0% gels were loaded onto a water-cooled, vertical, separating apparatus, from Owl Separations Systems™. The gels were prepared on an Owl Separation™ gel caster; gel and solution composition used for electrophoresis can be found in Appendix: B.  The top well and the bottom tray were both filled with 1X SDS/electrophoresis buffer.  The protein, already concentrated in 100 mM Tris-HCl buffer, was mixed with the sample buffer in 10:90 and 50:50 ratio (protein: sample buffer). The samples were then boiled in a water bath for three minutes to assure protein denaturation.

The 15 µl of the protein in sample buffer were then loaded into the sample wells. Molecular weight markers (Sigma-Aldrich) prepared in sample buffer, were also added to a sample well.  The power supply was set at 30 mA and the electrophoresis was run for approximately three hours.  The gel was then placed in a staining solution and gently agitated overnight at room temperature.  The gel was then placed in a de-staining solution and gently agitated until the gel was clear except for the bands.

### 2.1.4      Sample preparation

Samples were prepared by dissolving fresh lyophilized LPO in 50 mM acetate buffer (pH=4.0), 100 mM Tris-HCl buffer (pH=7.0 to 9.5), and 100 mM CAPS buffer (pH=9.5 to 11.0) to a concentration between 5 µM and 15 µM.   The samples were placed in a 1-cm path length quartz cuvette and sealed with a rubber cap and parafilm.  The samples

were then purged with argon gas for 15 minutes to remove $O_2$. 1 mM sodium dithionite was prepared in a 1.5 ml plastic vial and then 3 μl were added to reduce LPO. Finally the sample was saturated with CO for 15 minutes to form the CO-LPO complex.

Used LPO was stored in 1.5ml plastic vials at –40.0 ˚C. The used LPO was thawed at room temperature and spun down for 30 min. at 6700 rpm with a high-speed centrifuge (Allegra 64R, Beckman Coultier) in order to remove sodium dithionite and to concentrate the enzyme in the desired buffer. After the first concentration the sample was dissolved in the desired buffer and then concentrated again. This was repeated several times.

## 2.2 Kinetics of the conversion of the intermediate to final state of reduced LPO.
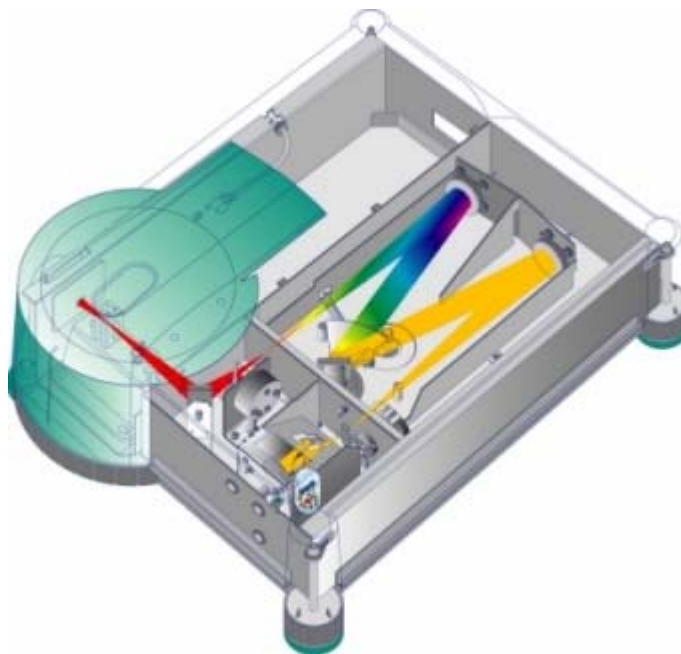
Figure 2.1: Scheme of the Varian (Cary 50), single beam spectrophotometer. The main components include: 150W Xe arc lamp, grating, and photodiode array detector.

UV-visible spectrophotometry (Figure 2.1) was used to measure the UV-visible steady state, as well as the kinetics of the intermediate ($Fe^{(II)}LPO$) to the final state ($Fe^{(II)}LPO$) conversion. The kinetics software package, Cary v3.0 (Varian) was used to record the change in absorbance at 434 nm over a 45-minute period. The kinetic traces represent the average absorbance every 30 seconds. Averaging time was set at 15 seconds.

Lactoperoxidase samples, dissolved in buffer (pH=7.0 to 11.0), were prepared in a 1-cm path length quartz cuvette. The cuvette was sealed with a rubber septum cap and

purged with Ar gas for 15 minutes. 4μl of 1mM sodium dithionite solution was then injected through the rubber septum cap to reduce the sample. The cuvette was shaken thoroughly for 5.0s. The sample was then placed in the UV-visible spectrophotometer and the change in absorbance was recorded using the Varian kinetics program. At the end of the data collection the trace was subsequently saved as an ASCII file and fit with a second order exponential decay equation, using Origin 5.0.

The traces were fit using a second order exponential decay model:

$$y = y_0 + A_1 e^{(-(x-x_0)/t_1)} + A_2 e^{(-(x-x_0)/t_2)} \tag{1}$$

Where y is the absorbance and x is the time. The lifetimes of the fast phase and the slow phase are $t_1$ and $t_2$, respectively. $A_1$ is the amplitude of the fast phase and $A_2$ is the amplitude of the slow phase. $x_0$ is the value of 0 at t=0 and $y_0$ is the absorbance at t=0. The percent amplitudes were calculated from the following equation:

$$\%A_{1 \text{ or } 2} = [A_{1 \text{ or } 2}/(A_1 + A_2)]*100 \tag{2}$$

The percent amplitudes of the fast and slow phases were plotted as a function of pH. The data points were then fit using Origin 5.0 with a modified Henderson-Hasselbalch equation:

$$y = a_{max} + ((a_{min} - a_{max})*(10^{(x-pKa)})/(1 + 10^{(x-pKa)})) \tag{3}$$

Where y is the percent amplitude, x is the pH, $a_{max}$ and $a_{min}$ are the maximum and minimum of the curve.

## 2.3  Determination of CO Binding Constant

Reduced LPO was prepared as per section 2.1.4 and was titrated with 5 μl additions of the 1 mM CO/100 mM Tris-HCl buffer (pH=7.0). After each CO addition a spectrum was recorded. In general 20 additions resulted in LPO saturation. The reduced

LPO spectrum was subtracted from the final CO bound spectrum to obtain the optical difference spectra. The wavelength of the maximum absorption change was determined from the optical difference spectra and plotted as a function of CO concentration. The changes in absorbance were corrected for dilution according to equations 4 and 5.

$$\Delta A \cdot d_f = \Delta A' \tag{4}$$

$$d_f = \frac{V_i + V_a}{V_i} \tag{5}$$

$\Delta A$ is the change in absorbance and $d_f$ is a dilution factor that corrects for the change in absorption due to the addition of the 1mM CO buffer. $\Delta A'$ is the corrected change in absorbency. In equation 3, $V_i$ is the initial volume in the cuvette and $V_a$ is the amount of 1 mM CO added. $\Delta A'$ was plotted as a function of CO concentration. The data was fit with a 3-parameter equation, using Origin 5.0.

$$\Delta A' = \frac{K_b \Delta \varepsilon c [CO]}{1 + K_b [CO]} \tag{6}$$

Where $K_b$ is the binding constant, [CO] is the concentration of CO, $\varepsilon$ is the molar absorbtivity, A' is the corrected absorbency, and c is the concentration of LPO. [39]

## 2.4    Measurement of kinetics of CO rebinding to Fe$^{(II)}$LPO

Transient absorption spectroscopy was used to measure the rate constant of CO rebinding to LPO.  Photodissociation of CO from the active site was achieved using a Continuum, Minilite II, Q-switched, Nd:YAG laser ($\lambda$=532 nm and E=20 mJ). The repetition rate of the laser was set at 1 Hz with a pulse width of 7 ns.   The optical path of our instrument is shown in Figure 2.2. The laser pulse was reflected off of two mirrors before passing through the sample in the cuvette holder.
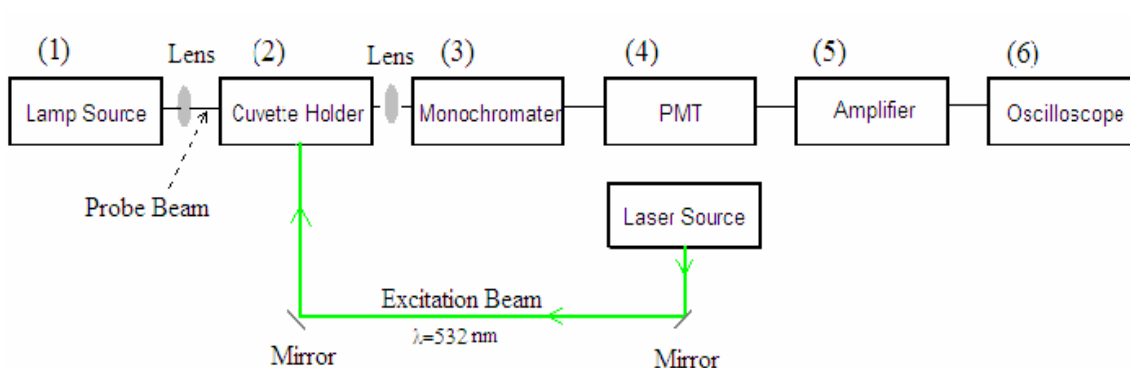


Figure 2.2: Instrumentation set-up for transient absorption spectroscopy.

Output from the 150W Xe arc lamp (Thermo-Oriel, model: 66902) was focused in the middle of the sample, contained in the temperature controlled cuvette holder (Flash 200, Quantum Northwest, accuracy: ±0.02°C).  The output from the sample was then focused on the input of a monochromater (Jobin Yvon, model: 0013-11-04) and detected by a PMT (H6780, Spectra-Physics) coupled to a high-gain amplifier (Thermo-Oriel, model: 70710).  The signal was then digitized by an oscilloscope (100 MHz, Tektronix TDS2012) and saved as an ASCII file.  The kinetic traces were recorded at 444 nm and

averaged for 30 to 50 pulses, providing an adequate S/N ratio. The kinetic traces were then fit with either a first or second order exponential decay, using Origin 5.0.

## 2.5    Photoacoustic Calorimetry (PAC):

### 2.5.1    PAC theory

Photothermal methods are based on the conversion of electromagnetic energy to mechanical energy. Through optical absorption, a molecule (gas, liquid, or solid) is photo-excited. The molecule subsequently relaxes to its ground-state energy level via fluorescence (stimulated or spontaneous emission), phosphorescence (spontaneous emission of long lived triplet-states), vibrational/rotational relaxation, collisional energy transfer, and or photochemical reactions.  The molecules that have relaxation pathways that emit radiation with a quantum yield ($\Phi$) of unity do not result in the conversion of light energy to mechanical energy and cannot be used for PAC [36, 37].  However, molecules that undergo photochemical reactions and or vibrational degradation (from vibrational relaxation and collisions) release heat (Q) within the illuminated volume which results in a change in temperature ($\Delta T$).  In such a case, thermodynamic parameters ($\Delta H$, $\Delta V$, $\Delta \rho$, $\Delta c$) for these processes can be measured by PAC. $\Delta H$ is the enthalpy change of the reaction, $\Delta V$ is the change in volume, $\Delta \rho$ is the change in density, and $\Delta c$ is the change in concentration [36, 37].

The change in heat is related to the temperature change through the heat capacity ($C_p$), and to the volume change through the isobaric expansion coefficient ($\beta$).  The change in volume then results in a pressure change ($\Delta P$) and these two quantities are related by the isothermal compressibility ($K_T$).  The relation of the change in heat to the change in pressure is shown in Figure 2.3.

$$VCp\rho \quad \beta = \frac{1}{V}\left(\frac{\partial V}{\partial T}\right)_P \quad K_T = \frac{1}{V}\left(\frac{\partial V}{\partial P}\right)_T$$

$$Q \longrightarrow \Delta T \longrightarrow \Delta V \longrightarrow \Delta P$$

Figure 2.3: Relationship for the conversion of the change in heat to the change in pressure [36].

Other contributions to the change in volume ($\Delta V_{con}$) come from stuctural rearrangements of the solution. Structural rearrangements are attributed to solvation of molecules, electrostriction, proton transfer, proton release, proton uptake, and, in the case of proteins, conformational changes [39]. The volume change, from both the change in heat and the structural rearrangements, results in a pressure wave. The pressure wave/acoustic wave is then converted into an electical signal using a piezoelectric transducer. The acoustic wave propagating from the reaction volume is shown in Figure 2.4.
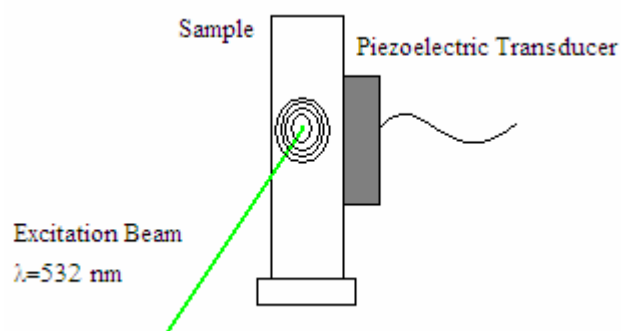


Figure 2.4 Acoustic wave generated in sample by laser pulse excitation beam.

The piezoelectric transducer is made of crystals of lead-zirconate-titanate that form an electric field when mechanical force is applied to it. Electric dipoles of the crystals are sensitive to mechanical stress and changes in the pressure results in electric output.
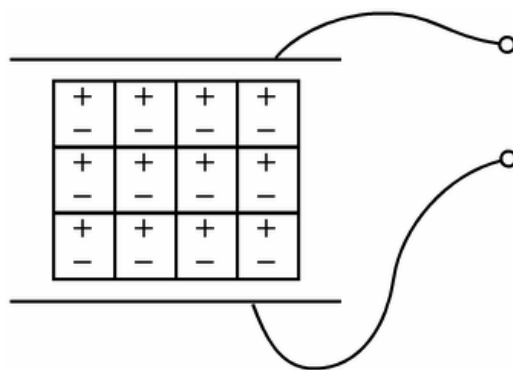


Figure 2.5 Generic example of a piezoelectric transducer. Mechanical force will distort the alignment of the dipoles forming an electric current between the electrodes.

### 2.5.2   Acoustic Wave Analysis

The acoustic signal generated from the photo-excited sample is described by the following equation:

$$S = K\ E_a(\Delta V_{th} + \Delta V_{con}) \tag{7}$$

S is the acoustic signal, K is an instrument response parameter, $E_a$ is the number of Einstein's absorbed, $\Delta V_{th}$ is the change in volume due to change in heat of the solution, and $\Delta V_{con}$ is the change in volume due to conformational changes. $\Delta V_{con}$ includes volume changes due to protein conformational changes, electrostriction, CO solvation, etc. $\Delta V_{th}$ originates from changes in the solvent due to thermal expansion and can be represented by the following equation:

$$\Delta V_{th} = (\beta / C_p \rho)Q \tag{8}$$

$C_p$ is the heat capacity of the solvent ($cal \cdot g^{-1} \cdot K^{-1}$), $\rho$ is the density of the solvent ($g \cdot ml^{-1}$), and $\beta$ is the expansion coefficient of the solvent ($K^{-1}$). Q is the heat released to the solvent subsequent to photoexcitation. Substitution of equation 2 into equation 1 gives the following:

$$S = K\, E_a[(\beta/C_p\rho)Q + \Delta V_{con}] \tag{9}$$

In order to resolve the enthalpy and volume changes of the photochemical reaction a reference compound must be used [36]. Photoexcitation of the reference compound does not result in any chemical reaction and all energy absorbed degrades to the solution as heat, and thus, $\Delta V_{con}$ is 0. The resulting acoustic signal can be represented by the following equation:

$$R = KE_aE_{hv}(\beta/C_p\rho) \tag{10}$$

Where R is the acoustic signal of the reference sample and $E_{hv}$ is the energy of the laser. In our measurements we have used $Fe^{(III)}$meso-tetra(4-sulfonatophenyl)porphyrin chloride (4sp) as a reference compound. The volume and enthalpy changes can be found by taking the ratio of Equation 9 to Equation 10. The instrument response parameter cancels out and the following equation is obtained:

$$(S/R)\, E_{hv} = [Q + (C_p\rho/\beta)\, \Delta V_{con}] \tag{11}$$

The volume and enthalpy changes can be found from the slope and intercept, respectively, of the plot of $(S/R) \cdot E_{hv}$ versus $(C_p\rho/\beta)$. The intercept is the total heat change for the system and for processes faster than 50 ns (the resolution of the instrumentation) the enthalpy must be solved from the following equation:

$$\Delta H\, \Phi = E_{hv} - Q \tag{12}$$

The change in volume must be corrected for the quantum yield as well:

$$\Delta V \Phi = \Delta V' \tag{13}$$

Where $\Delta V$ comes from the slope of the curve and $\Delta V'$ is the corrected change in volume [39]. Samples for PAC were prepared as described in section 2.1.4 in concentrations ranging between 10 $\mu M$ and 20 $\mu M$. The reference compound was prepared by dissolving 4sp in the identical buffer that the sample was prepared in. 4sp fulfills the requirements for a reference compound.

### 2.5.3 Determination of $C_p\rho/\beta$ for buffers with high ionic concentrations

$C_p\rho/\beta$ is strongly affected by the composition of the solvent. Therefore the value of $C_p\rho/\beta$ for solvents with higher ionic concentration had to be measured.

PAC waveforms were collected for 0 mM, 100 mM, 250 mM, and 500 mM NaCl concentrations at the following temperatures: 14, 16, 18, 20, 22, 24, 26, and 32 °C. Therefore, equation 8 can be used to describe the acoustic wave for both the ionic sample and reference sample. Since $C_p\rho/\beta$ is known for the reference sample in $H_2O$, by taking the ratio of sample to reference, the $C_p\rho/\beta$ for the buffer with a different ionic concentration can be calculated for [40].

$$\frac{R_{100\,mM} = KE_a\,E_{hv}\Phi(\beta/C_p\rho)_{100mM}}{R_{0\,mM} = KE_a\,E_{hv}\Phi(\beta/C_p\rho)_{0mM}} \tag{14}$$

Which gives,

$$\frac{R_{100\,mM} = (\beta/C_p\rho)_{100mM}}{R_{0\,mM} = (\beta/C_p\rho)_{0mM}} \tag{15}$$

$$\frac{R_{100\,mM}(\beta/C_p\rho)_{0mM}}{R_{0\,mM}} = (\beta/C_p\rho)_{100mM} \tag{16}$$

## 2.5.4  PAC instrumentation
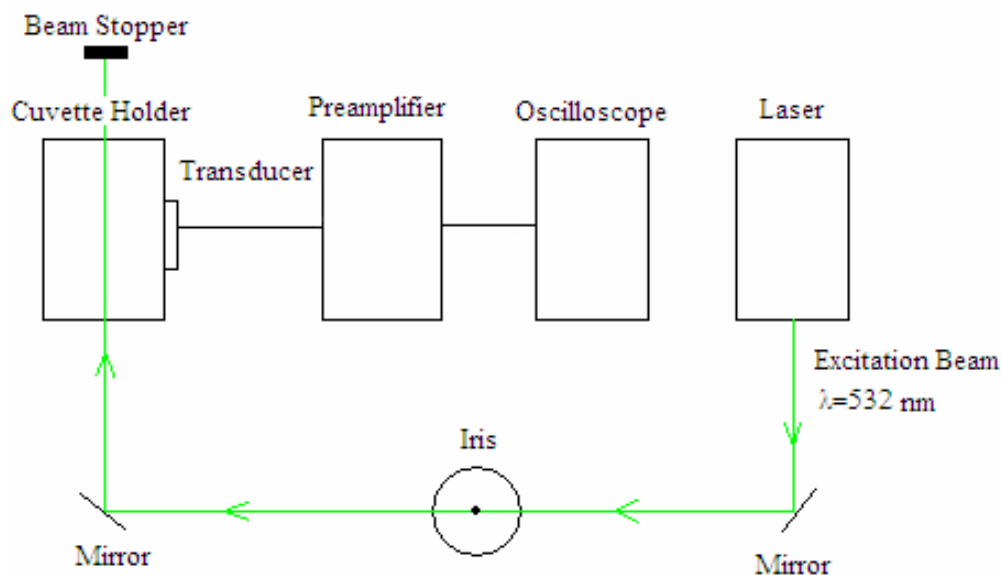


Figure 2.6: Instrumentation set-up for photoacoustic calorimetry.

The instrumentation setup for photoacoustic calorimetry is shown in Figure 2.6. Photoexcitation of the sample was achieved with a Nd:YAG laser, Continuum, Minitlite II.  The doubling frequency of the laser was 532 nm and the laser pulse width was 7 ns. The energy of the laser for PAC measurements was set at 50 µJ. The optical path of the laser is shown in Figure 2.6.  An iris was used to adjust the diamter of the laser beam to 1mm to improve the time resolution of the instrumentation.  The sample was contained within a temperature controlled cuvette holder (Quantum Northwest). The acoustic signal was detected with a 1MHz piezoelectric transducer (TR-V103, Panametrics).  The transducer was attached to the side of the cuvette with a thin layer of vacuum grease to facillitate the coupling. 30 to 50 laser pulses were averaged to improve the S/N ratio.  The signal was digitized by a 500MHz Tektronix (model: TDS 544A) oscilloscope.

# 3.0   Results

## 3.1   Electrophoresis Results

SDS–Page electrophoresis was used to determine the purity of native bovine lactoperoxidase purchased from Worthington and Sigma-Aldrich. Figure 3.1 shows the UV-visible spectrum of $Fe^{(III)}LPO$. The purity of the sample was estimated by taking the ratio of the absorbance of the Soret maximum ($\lambda$=412 nm) to the absorbance at 280 nm. Samples with an RZ value ($RZ=A_{412}/A_{280}$) greater than 0.8 were used in all experiments. Along with the fresh samples, a used sample was analyzed to make sure that the centrifuged protein maintained its integrity. In Figure 3.2, sample well A contained the used LPO, wells B and C contained Worthington LPO, well D contained the marker, and wells E and F contained the LPO from Sigma-Aldrich.  The highest weight for the marker was 66,000 Da, which is less than the molecular weight of LPO (80,000 Da). High protein concentrations caused the samples to pinch the marker column and cause the marker bands to bend.  The samples did not appear to be able to mix with neighboring sample wells. SDS-Page electrophoresis analysis shows that enzymes purchased from the two companies are the same and the used LPO maintained its integrity.
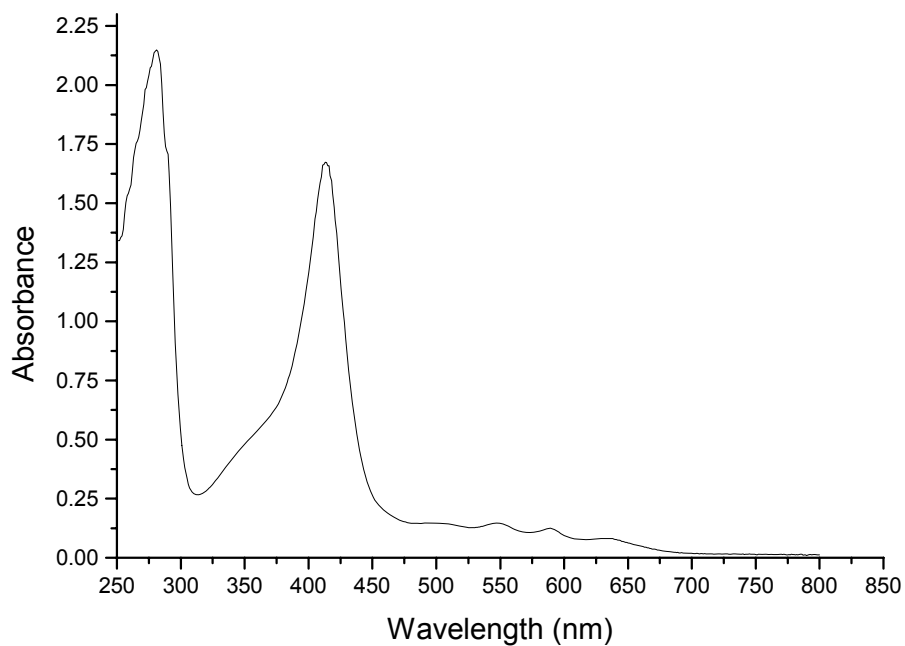
Figure 3.1: UV-visible spectrum of Fe$^{(III)}$LPO in 100 mM Tris-HCl (pH=7.0).
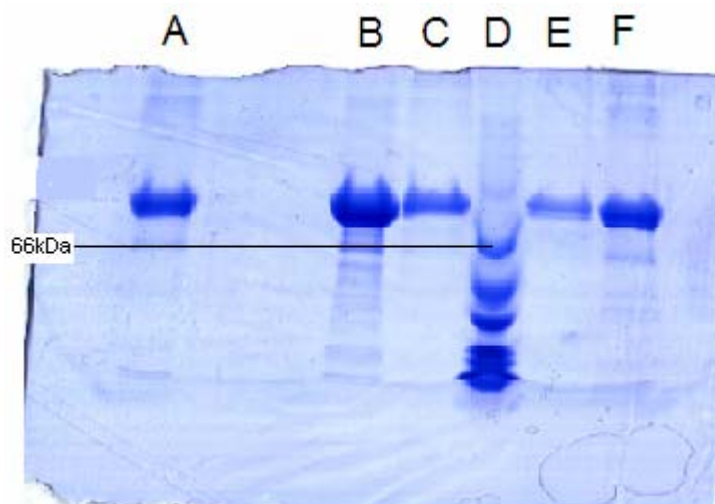


Figure 3.2: 10% polyacrylamide gel, SDS-PAGE. See section 3.1 for details. Sample well A: used LPO; well B and C: LPO from Worthington, well D: markers of molecular mass; 66, 45, 36, 29, 24, 20.1, and 14.2 kDa. Wells E and F contained protein from Sigma-Aldrich.

## 3.2     Results of Steady-state UV-visible Spectroscopy

It has been shown previously that $Fe^{(III)}LPO$ exhibits a Soret band at 412 nm that is red shifted (7-10 nm) compared to other high-spin heme proteins with Q bands at 497, 542, 587, and 630 nm. The extinction coefficient of these bands are slightly more enhanced as well [34].  Figure 3.3 displays the typical absorption spectra for $Fe^{(III)}LPO$, $Fe^{(II)}LPO_{intermediate}$, $Fe^{(II)}LPO_{final}$, and CO-LPO, in 100 mM sodium phosphate buffer (pH=7.0). Upon reduction with sodium dithionite, LPO quickly assumes a conformation with a Soret maximum at 447 nm, with visible bands located at 561 and 596 nm. This intermediate is short-lived and the Soret peak shifts to 433 nm indicating the formation of $Fe^{(II)}LPO_{final}$ state. The 433 nm peak is broad, which indicates that reduced LPO exists in equilibrium between two different conformations, as suggested previously [35].  The change in the visible bands as the Soret peak shifts is shown in Figure 3.4. As the final $Fe^{(II)}LPO$ conformation equilibrates, there is a decrease in the absorption peak at 596 nm and a slight increase in the absorption peak at 561 nm.  After purging $Fe^{(II)}LPO_{final}$ with CO for 10-30 minutes, the Soret peak shifts to 425 nm with $\alpha$ and $\beta$ bands at 541 and 576 nm, respectively. The CO-LPO spectra are shown in Figure 3.5 and the visible bands are shown in Figure 3.6.  There was no difference in the CO-LPO complex formed when $Fe^{(II)}LPO_{intermediate}$ or $Fe^{(II)}LPO_{final}$ was purged with CO. The spectral properties for the different LPO adducts at pH=4.0, 7.0, and 10.0 are listed in Table 3.1.

**Table 3.1** Spectroscopic characterization of ferric, ferrous and CO-LPO.

| pH | Complex | Soret maximum (nm) | Visible bands maxima (nm) |
|---|---|---|---|
| 4.0 | Fe$^{(III)}$LPO | 412 | 498, 542, 587, 627 |
|  | Fe$^{(II)}$LPO $_{intermediate}$ | N/A |  |
|  | Fe$^{(II)}$LPO$_{final}$ | 433 | 561, 596 |
|  | CO-LPO | 425 | 540, 575 |
| 7.0 | Fe$^{(III)}$LPO | 412 | 498, 542, 588, 630 |
|  | Fe$^{(II)}$LPO $_{intermediate}$ | 447 | 561, 596 |
|  | Fe$^{(II)}$LPO$_{final}$ | 433 | 561, 596 |
|  | CO-LPO | 425 | 541, 576 |
| 10.0 | Fe$^{(III)}$LPO | 412 | 498, 542, 585, 630 |
|  | Fe$^{(II)}$LPO $_{intermediate}$ | 447 | 560, 596 |
|  | Fe$^{(II)}$LPO$_{final}$ | 433 | 558, 596 |
|  | CO-LPO | 430 | 546, 575 |

Fe$^{(III)}$LPO in 50 mM acetate buffer (pH=4.0) has a spectrum similar to that of Fe$^{(III)}$LPO at pH=7.0 and is shown in Figure 3.5. The Soret maximum of Fe$^{(III)}$LPO is located at 412 nm and the visible bands are at 498, 542, 587 and 630 nm. Reduction with sodium dithionite caused the Soret maximum to immediately shift to 433 nm with visible bands at 561 and 596nm. The Fe$^{(II)}$LPO$_{final}$ spectrum is shown in Figure 3.5. The intermediate reduced complex of LPO was not seen. Fe$^{(II)}$LPO$_{final}$ complex at pH < 7.0 becomes increasingly unstable and oxidizes easily. However, The CO-LPO complex (spectra shown in Figure 3.5) is stable at pH < 7.0. Therefore, CO-LPO samples at pH=4.0 were prepared by purging Fe$^{(III)}$LPO with CO prior to reduction with sodium dithionite.

At pH=10.0, the Fe$^{(III)}$LPO complex and the Fe$^{(II)}$LPO$_{final}$ complex had similar spectra to that of the pH=4.0 and 7.0 complexes. The steady state spectra of Fe$^{(III)}$LPO, Fe$^{(II)}$LPO$_{intermediate}$, Fe$^{(II)}$LPO$_{final}$, and CO-LPO in at pH=10.0 is shown in Figure 3.6. However, the CO-LPO complex spectra were significantly different. The Soret peak at pH=10.0 compared to pH=4.0 and 7.0 was red shifted by 5 nm. The visible bands were

significantly broader than at pH=4.0 or 7.0. The overlay of the CO-LPO spectra measured

at pH=4.0, 7.0, and 10.0 is shown in Figure 3.7 and 3.8.
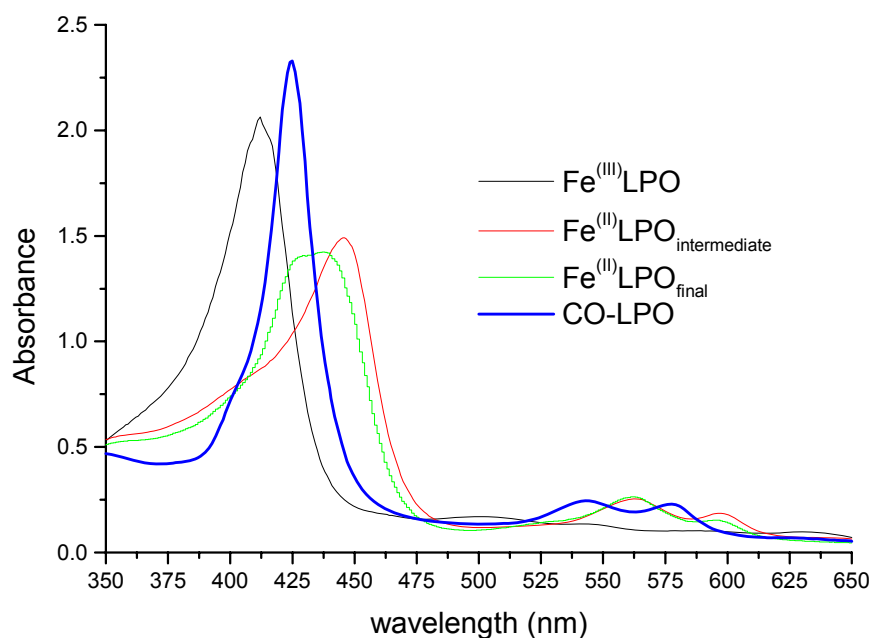


Figure 3.3: Overlay of the steady state absorption spectra of Fe$^{(III)}$LPO (black), Fe$^{(II)}$LPO$_{intermediate}$ (red), Fe$^{(II)}$LPO$_{final}$ (green), and CO-LPO (blue). Sample in 100 mM sodium phosphate buffer (pH=7.0).
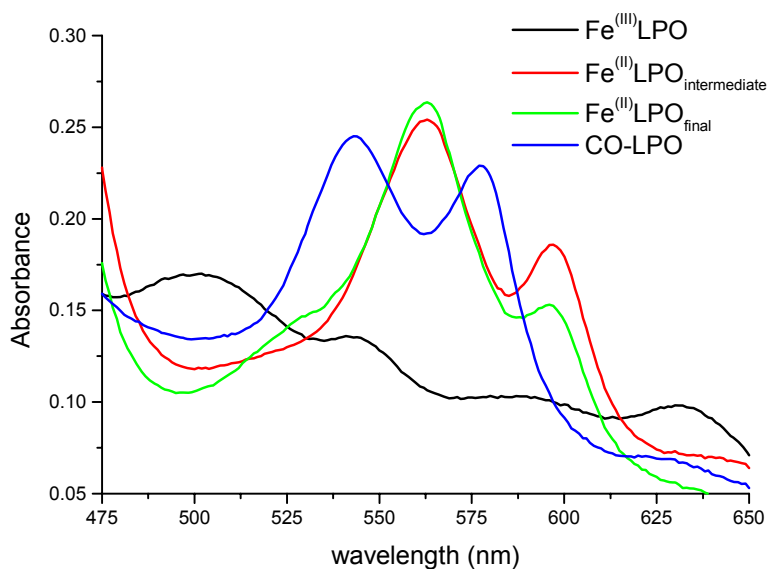


Figure 3.4: Overlay of the visible absorption spectra of Fe$^{(III)}$LPO (black), Fe$^{(II)}$LPO$_{intermediate}$ (red), Fe$^{(II)}$LPO$_{final}$ (green), and CO-LPO (blue). Sample in 100 mM sodium phosphate buffer (pH=7.0).
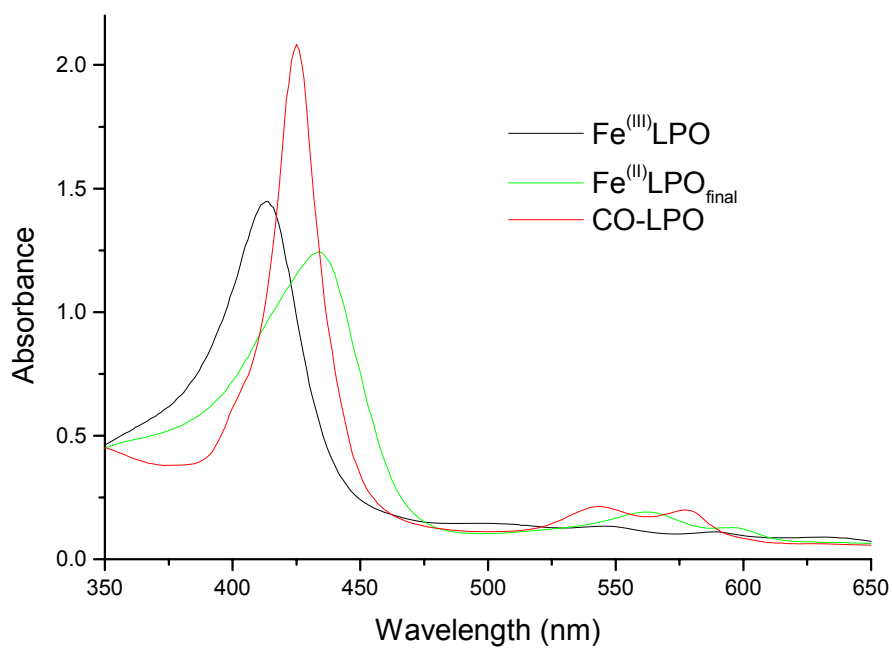
Figure 3.5 Overlay of the steady state absorption spectra of $Fe^{(III)}LPO$ (black), $Fe^{(II)}LPO_{final}$ (green), and CO-LPO (red). Sample in 50 mM acetate buffer (pH=4.0).
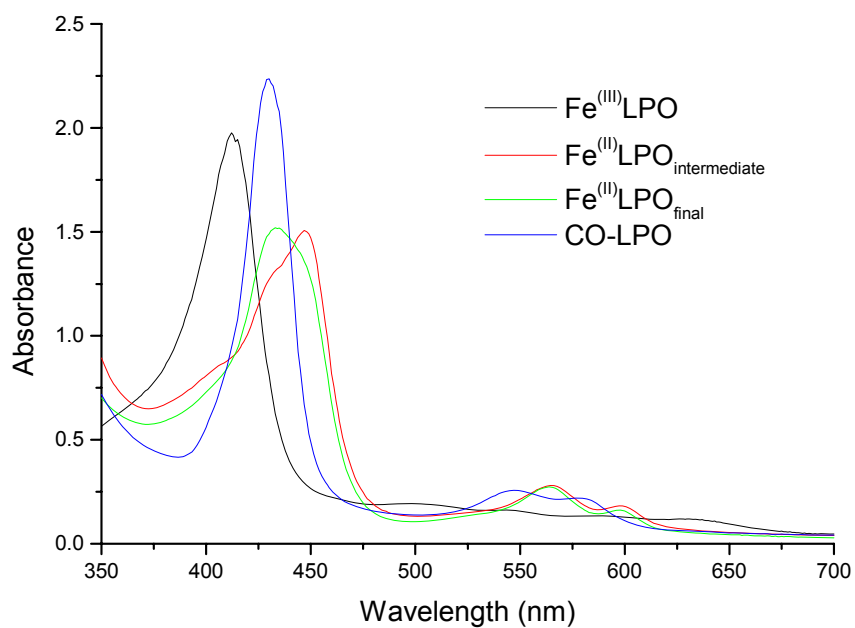


Figure 3.6: Overlay of the steady state absorption spectra of $Fe^{(III)}LPO$ (black), $Fe^{(II)}LPO_{intermediate}$ (red), $Fe^{(II)}LPO_{final}$ (green), and CO-LPO (blue). Sample in 100 mM CAPS buffer (pH=10.0).
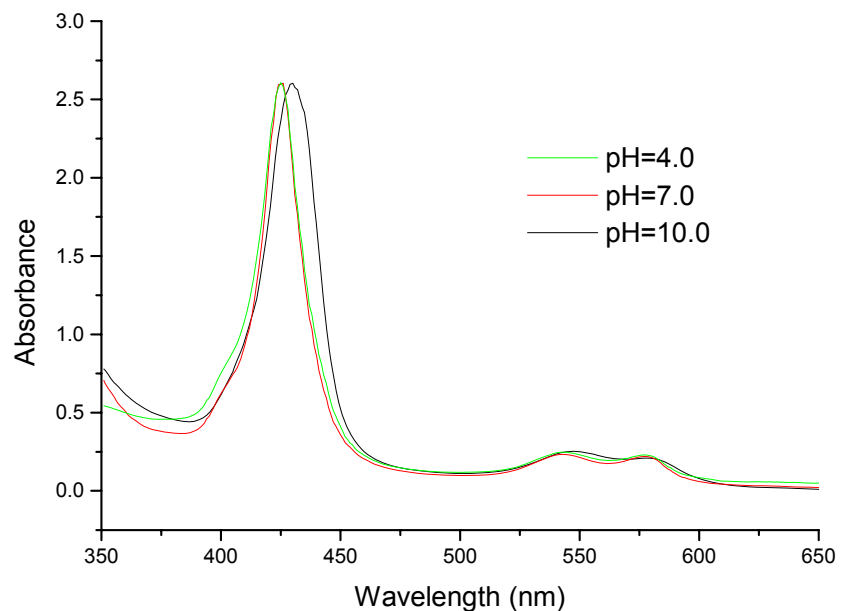
Figure 3.7: Overlay of the steady state absorption spectra of CO-LPO at pH=4.0 (green), 7.0 (red), and 10.0 (black).
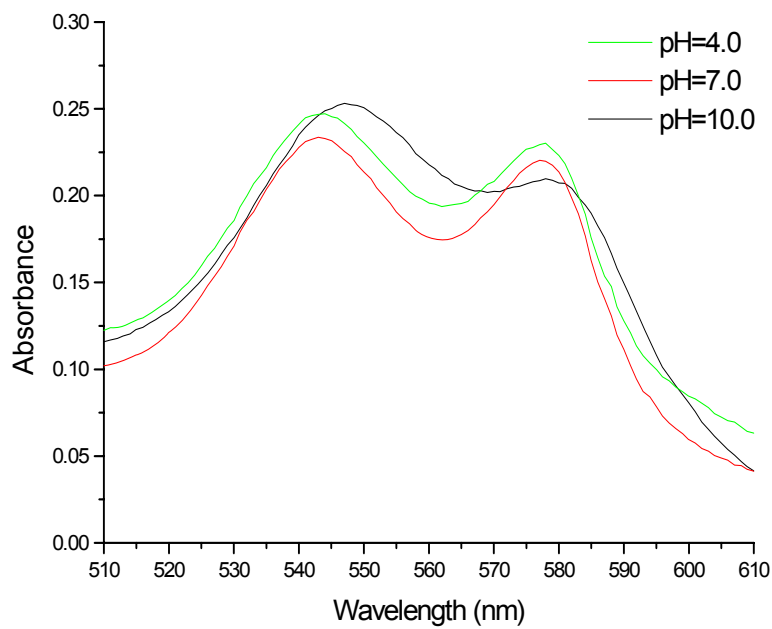


Figure 3.8: Overlay of the steady state absorption spectra visible bands of CO-LPO at pH=4.0 (green), 7.0 (red), and 10.0 (black).

## 3.3 Measurement of the Intermediate Kinetics results.

The kinetics of formation of the $Fe^{(II)}LPO_{final}$ state was measured using steady-state UV-visible spectroscopy and were found to be a pH dependant, biphasic process. Figure 3.9 shows the overlay of the steady state spectra of $Fe^{(II)}LPO$ during conversion, collected every two minutes. The overlay exhibits several isosbestic points suggesting that there are only two absorbing species during the reaction. To determine the rate constant of transition, the absorbance was measured at 434nm as a function of time (in minutes). Figure 3.10 shows the kinetic traces for transition of $Fe^{(II)}LPO_{intermediate}$ to $Fe^{(II)}LPO_{final}$ in the pH range from pH=7.0 to pH=11.0.

The best fit of the traces was obtained using a second order exponential decay, indicating that the conversion from $Fe^{(II)}LPO_{intermediate}$ to $Fe^{(II)}LPO_{final}$ is a biphasic process. Increase in pH resulted in a slower conversion. However, when the lifetimes of the fast phase and slow phase were plotted as a function of pH, no significant pH dependence was observed (Figure 3.11). The plot of the percent amplitudes for the fast and slow phase did show significant pH dependence, shown in Figure 3.12. The plots of the percent amplitude for the fast and slow phases as a function of pH were fit with a modified Henderson-Hasselbalch equation. The fits for the fast and slow phases indicate a $pK_a$ of 9.1 and 9.3, respectively. The pH dependence of the fast and slow phase amplitudes for the conversion of $Fe^{(II)}LPO_{intermediate}$ to $Fe^{(II)}LPO_{final}$ suggest that the enzyme exists in two conformations with different rate constants for conversion. At neutral pH, the conformation with a fast rate constant is populated whereas at basic pH, the conformation with a low rate constant is stabilized. From the determined $pK_a$ values

of 9.1 and 9.3 we suggest that protonation of a residue or cluster of residues with a $pK_a$

close to 9.2 is associated with the transition between two conformations.
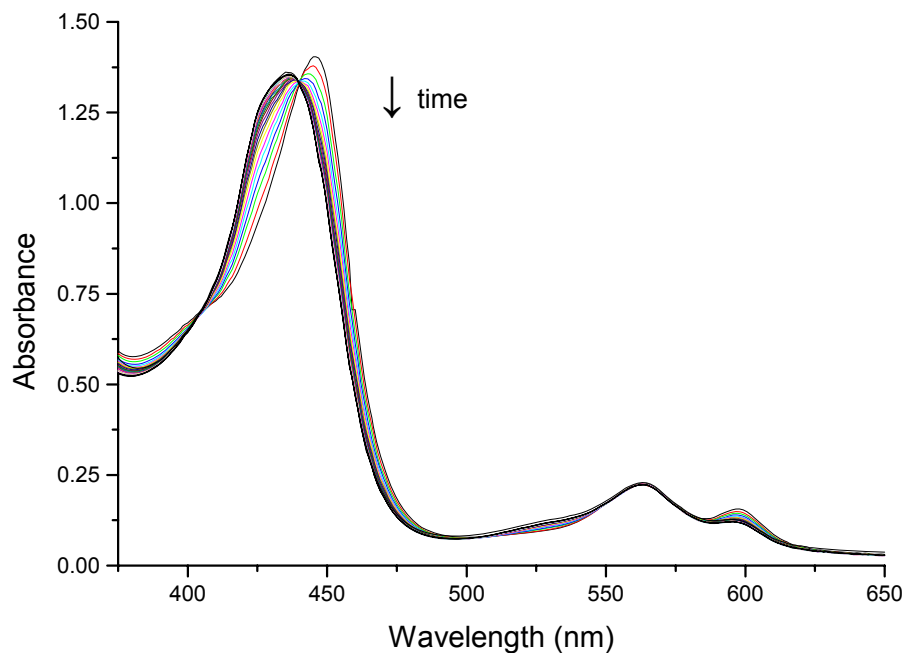


Figure 3.9: Overlay of the steady state spectra of Fe$^{(II)}$LPOintermediate conversion to Fe$^{(II)}$LPOfinal at pH=7.0. Spectra were collected every two minutes until the spectra ceased to change.
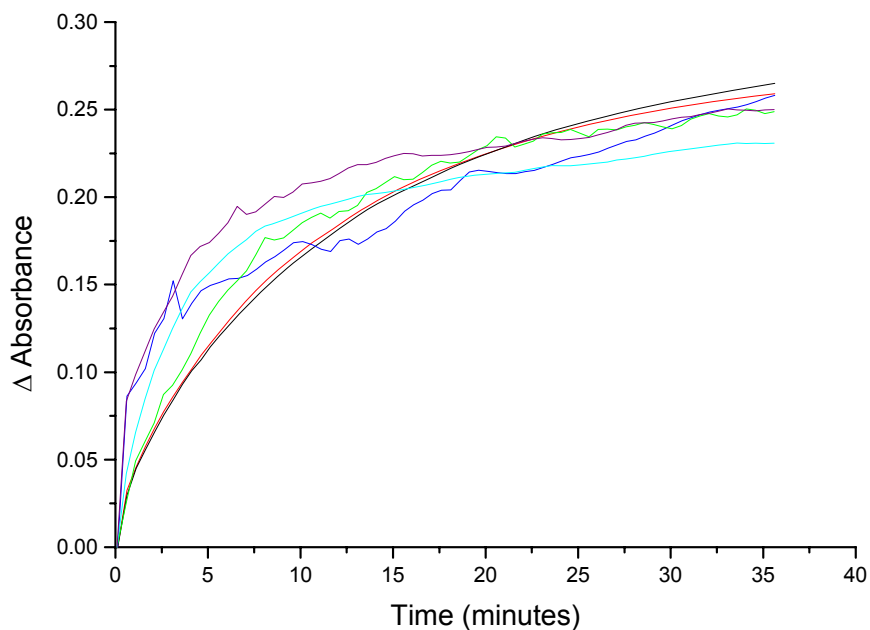


Figure 3.10: Traces of Fe$^{(II)}$LPO$_{intermediate}$ converting to Fe$^{(II)}$LPO$_{final}$ determined at pH=7.0, cyan; pH=8.0, green; pH=9.0, purple; pH=9.5, blue, pH=10.0, black; pH=11.0, red.
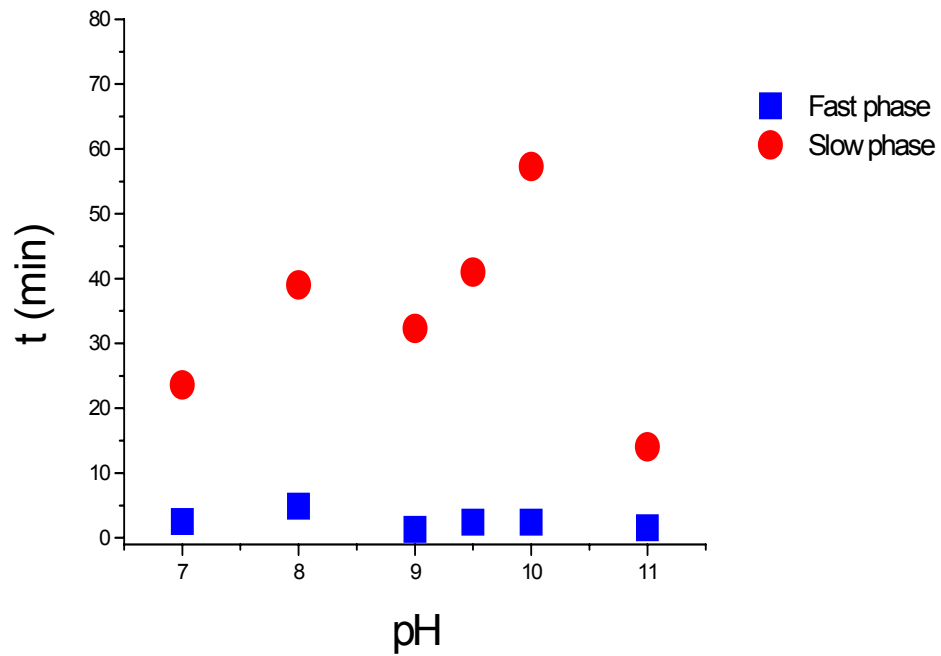
Figure 3.11: Plot of the rate of the fast and slow phases from the second exponential decay fits, plotted as a function of pH. The data in red corresponds to the slow phase and in blue to the fast phase.
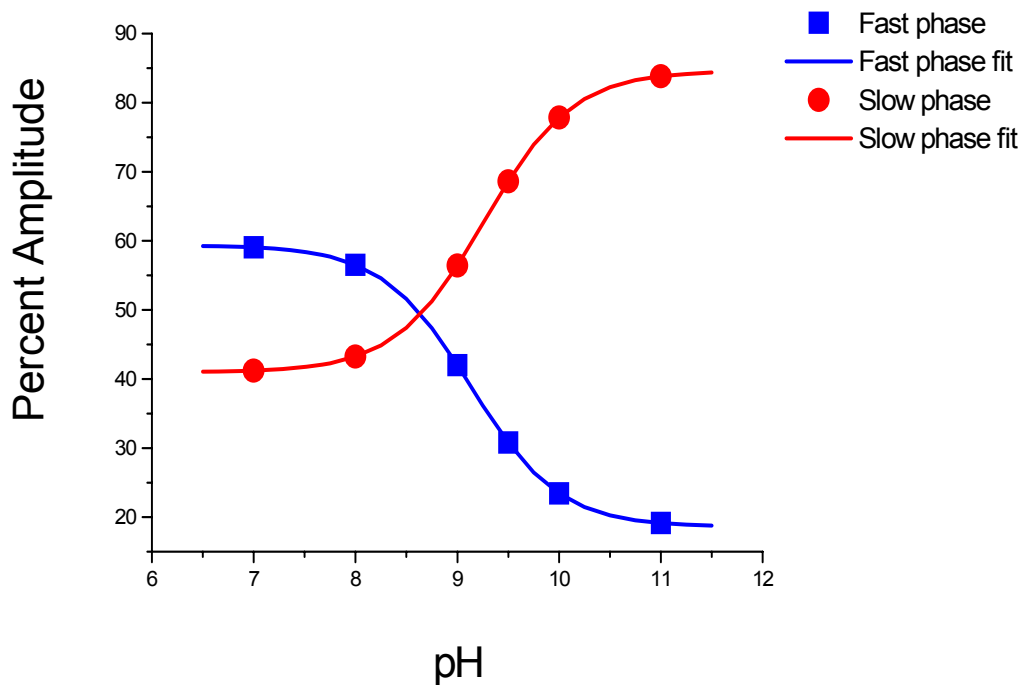


Figure 3.12: Plot of the percent amplitude of the fast and slow phases from the second exponential decay fits, plotted as a function of pH. The data in red corresponds to the slow phase and in blue to the fast phase.

## 3.4    Determination of the CO Binding Constant

Reduced LPO was titrated with 1 mM [CO]/100 mM Tris-HCl solution, as described in the Materials and Methods section 2.3. Figure 3.13 shows the titration curve, and the solid line corresponds to the fit using equation 6. The $K_b$ was 118 mM$^{-1}$, $\Delta\varepsilon = 130$ M$^{-1}$ cm$^{-1}$, and c = 6.3 µM.
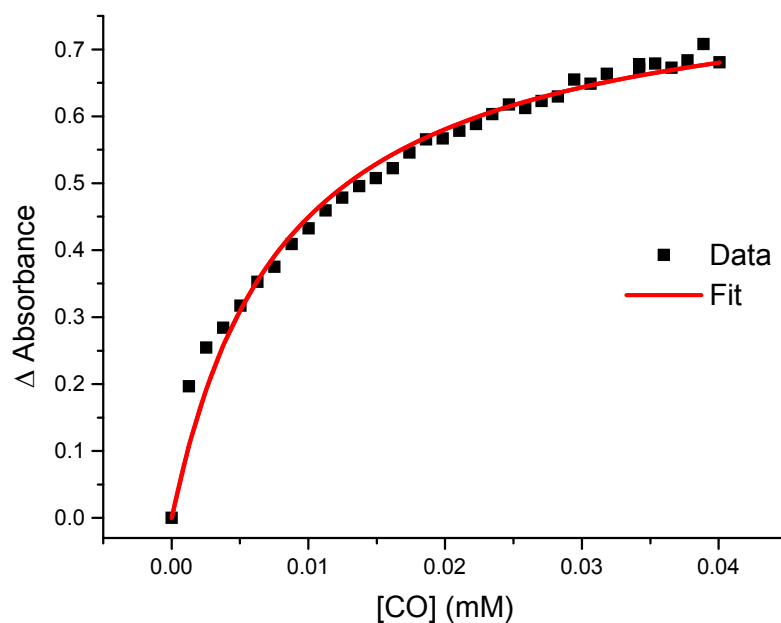


Figure 3.13: The change in corrected absorption plotted as a function of concentration of [CO].

## 3.5    Transient absorption results

$$P + L \longrightarrow P:L \longrightarrow PL$$
$$\quad\; 1 \qquad\qquad\quad 2 \qquad\qquad 3$$
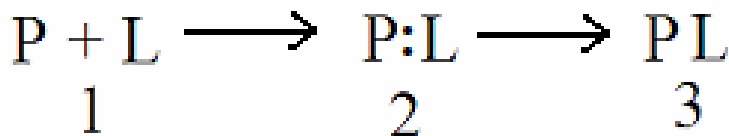
Figure 3.14: Reaction scheme for CO association to Fe$^{(II)}$LPO. P is the enzyme and L is the ligand. P+L represents the unbound enzyme and ligand. P:L is the geminate pair, where the ligand is in the active site but is not bound to the protein, and PL is the protein/ligand complex.

The reaction scheme in Figure 3.14 is used to describe the binding of CO to Fe$^{(II)}$LPO. The first step is CO binding to the protein, but remaining unligated to the heme. This is called the geminate pair (P:L). The next step is CO becoming covalently bound to the Fe$^{(II)}$LPO. The rate of CO-rebinding to Fe$^{(II)}$LPO after photodissociation, was measured using transient absorption as a function of temperature, at pH=4.0, 7.0, and 10.0. The spectra of CO rebinding to Fe$^{(II)}$LPO at pH=4.0 and 7.0 were fit with a first order exponential decay. At pH=10.0, however, CO rebinding was biphasic and satisfactory fit was obtained with a second exponential decay. The typical traces of CO rebinding to Fe$^{(II)}$LPO at 23ºC, at pH=4.0, 7.0, and 10.0 are shown in Figures 3.15, 3.16, 3.17, and 3.18, respectively.
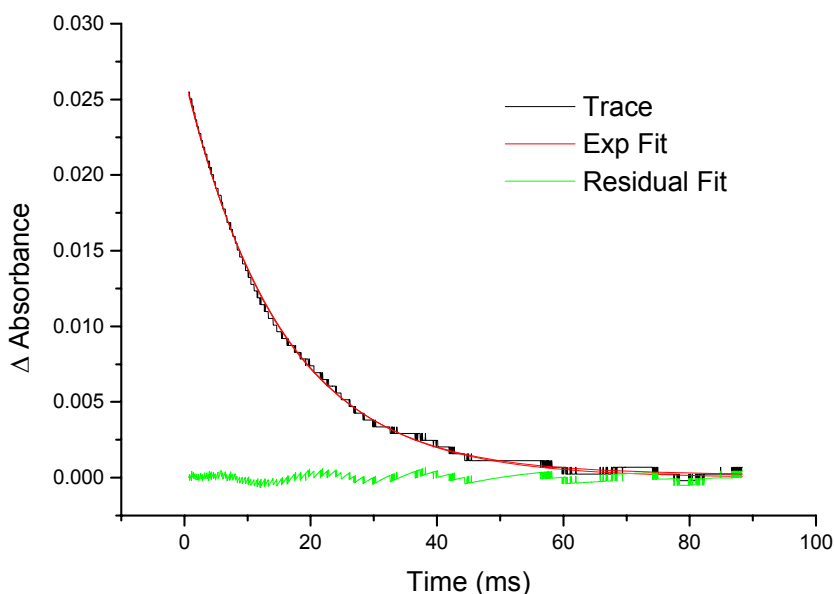


Figure 3.15: Transient absorption spectra of CO-LPO in 50mM acetate buffer (pH=4.0). Trace (black) first order exponential decay fit (red), residual (green).
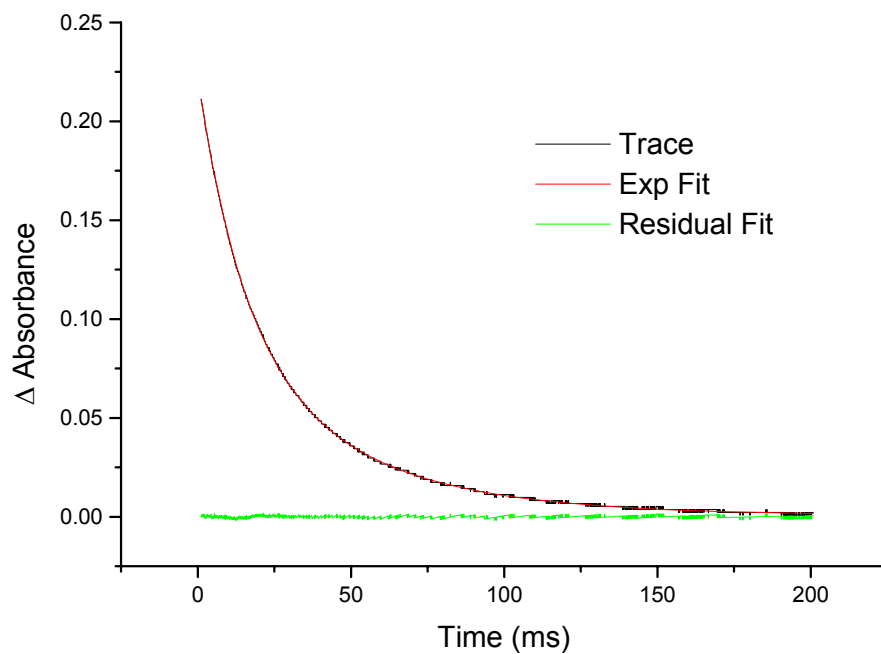
Figure 3.16: Transient absorption spectra of CO-LPO in 100mM Tris-HCl (pH=7.0). Trace (black), single exponential decay fit (red), residual (green).
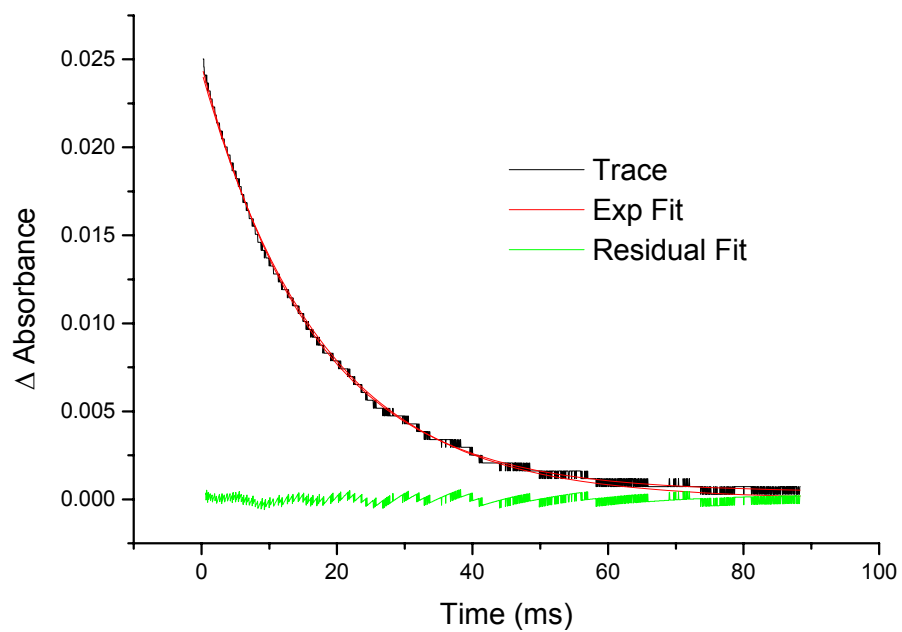


Figure 3.17: Transient absorption spectra of CO-LPO in 100mM sodium phosphate buffer (pH=7.0). Trace (black), single exponential decay fit (red), residual (green).
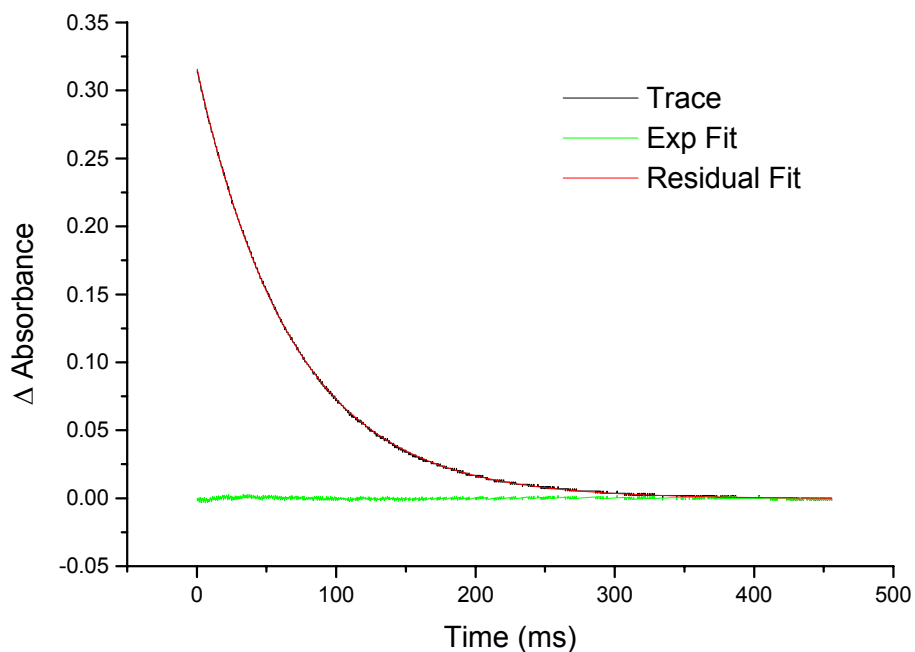
Figure 3.18: Transient absorption spectra of CO-LPO in 100mM CAPS buffer (pH=10.0). Trace (black), second order exponential decay fit (red), residual (green).

**Table 3.2:** Activation enthalpy, entropy and rate constant for CO rebinding to $Fe^{(II)}LPO$ at pH=4.0,7.0, and 10.0.

| Buffer | $\Delta H^{\neq}$ (kcal·mol$^{-1}$) | $\Delta S^{\neq}$ (cal·mol$^{-1}$ K$^{-1}$) | k (M$^{-1}$·s$^{-1}$) 23ºC |
|---|---|---|---|
| 50mM acetate (pH=4.0) | 8.3 ± 1.0 | -25.5 ± 1.1 | $2.7 \times 10^4$ |
| 100mM phosphate (pH=7.0) | 7.0 ± 0.4 | -27.2± 1.8 | $4.9 \times 10^4$ |
| 100mM Tris-HCl (pH=7.0) | 7.1 ± 0.5 | -26.9± 1.6 | $5.1 \times 10^4$ |
| 100mM Caps (pH=10.0) | fast 6.6 ± 2 | -20.8 ± 15.6 | $7.1 \times 10^4$ |
| | slow 3.3 ± 3 | -39.8 ± 5.8 | $1.3 \times 10^4$ |

The rate constants of CO rebinding to LPO at 23ºC are listed in Table 3.2. The pH increase resulted in an increase of the rate constant ~three times. And at pH=10.0 becomes bipahsic with a fast phase rate constant $7.1 \times 10^4$ M$^{-1}$·s$^{-1}$ and a slow phase rate constant $1.3 \times 10^4$ M$^{-1}$·s$^{-1}$. The corresponding percent amplitudes of the traces, $A_1$ and $A_2$, were 28% and 72%, respectively. From the recorded data, Eyring plots were constructed to determine the activation enthalpy and entropy for CO recombination. Typical Eyring

plots for CO rebinding to Fe$^{(II)}$LPO are shown in Figure 3.19. $\Delta H^{\neq}$ and $\Delta S^{\neq}$ at pH=4.0

and 7.0 were similar. At pH=10.0 the fast phase $\Delta H^{\neq}$ and $\Delta S^{\neq}$ were similar to that at

pH=4.0 and 7.0. Activation enthalpy and entropy for the slow was significantly smaller.
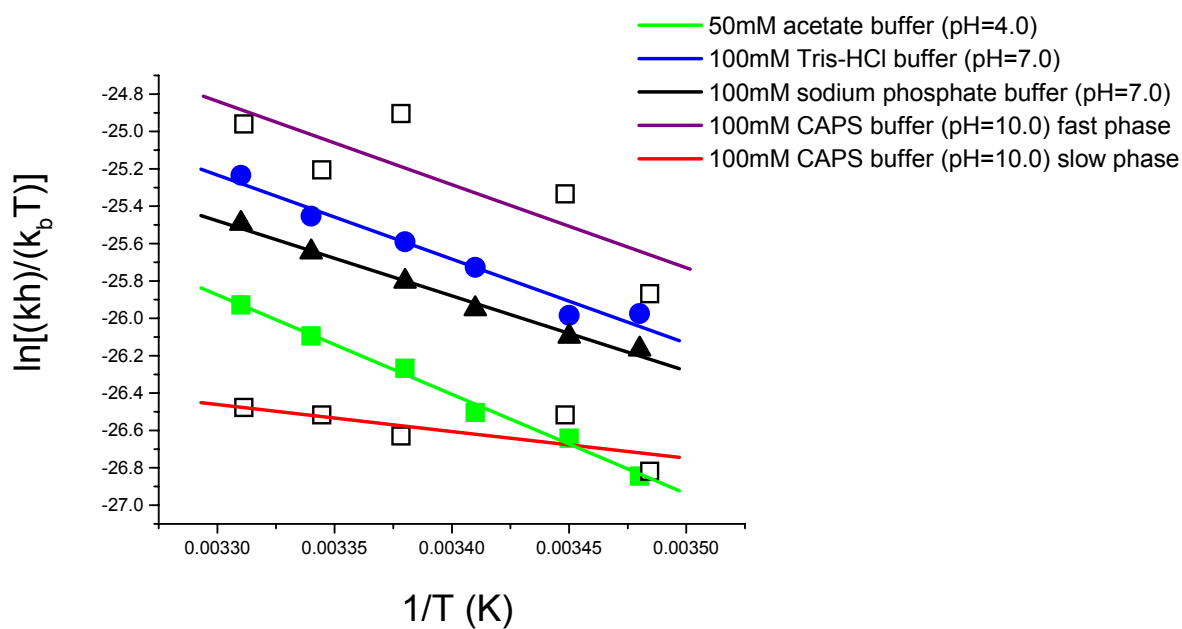


Figure 3.19: Eyring plots for CO rebinding to Fe$^{(II)}$LPO. 50mM acetate buffer (pH=4.0), green fit; 100mM sodium phosphate buffer (pH=7.0), blue fit; 100mM Tris-HCl buffer (pH=7.0), blue fit; 100mM CAPS buffer (pH=10.0), fast and slow phases, purple and red fits, respectively.

## 3.6 PAC Results

The photoacsoutic traces of the ligand photodissociation from CO-LPO in 100mM sodium phosphate buffer (pH=7.0) and 100mM Tris-HCl buffer (pH=7.0) are shown in Figures 3.20 and 3.21, respectively. The sample traces are overlaid with the reference compound traces. The reference compound releases the absorbed light energy to the solvent as heat, faster than the instrumentation response (~50 ns) and is used to calibrate the instrumentation. Data shows that the sample signal has an amplitude larger than the reference signal, but is not shifted in phase relative to the reference signal. The lack of shift in phase indicates that the reaction volume and enthalpy changes occur faster than 50 ns.
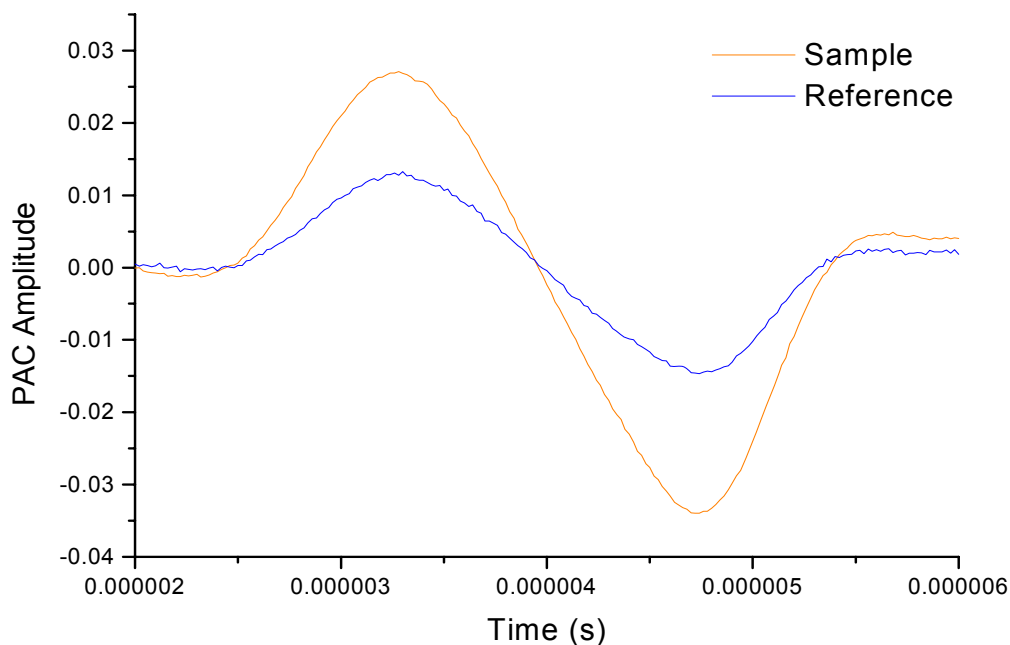


Figure 3.20: Overlay of the sample and reference acoustic waves for CO photodissociation from $Fe^{(II)}$LPO in 100mM sodium phosphate buffer (pH=7.0), 23 ºC. Sample wave (orange), reference wave (blue).
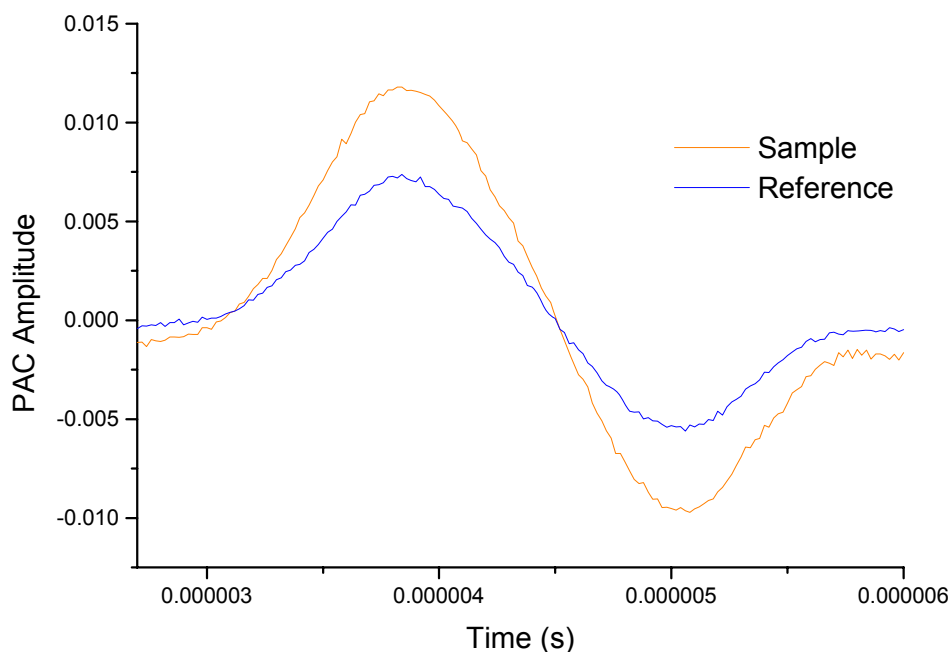
Figure 3.21: Overlay of the sample and reference acoustic waves for CO photodissociation from Fe$^{(II)}$LPO in 100mM Tris-HCl buffer (pH=7.0), 23 ℃. Sample wave (orange), reference wave (blue).

Figure 3.22 shows the overlay of the sample signal for the photodissociation of CO-LPO in 100mM Tris-HCl (pH=7.0) at temperatures: 14, 17, 20, 23, 26, and 29 °C. Figure 3.23 shows the temperature dependence of the acoustic signal for the reference compound. The wave profile for the sample and reference compounds stayed the same throughout the experiment indicating that the instrumentation (interface between the cuvette and the transducer) was not disturbed and that the sample did not become oxidized.
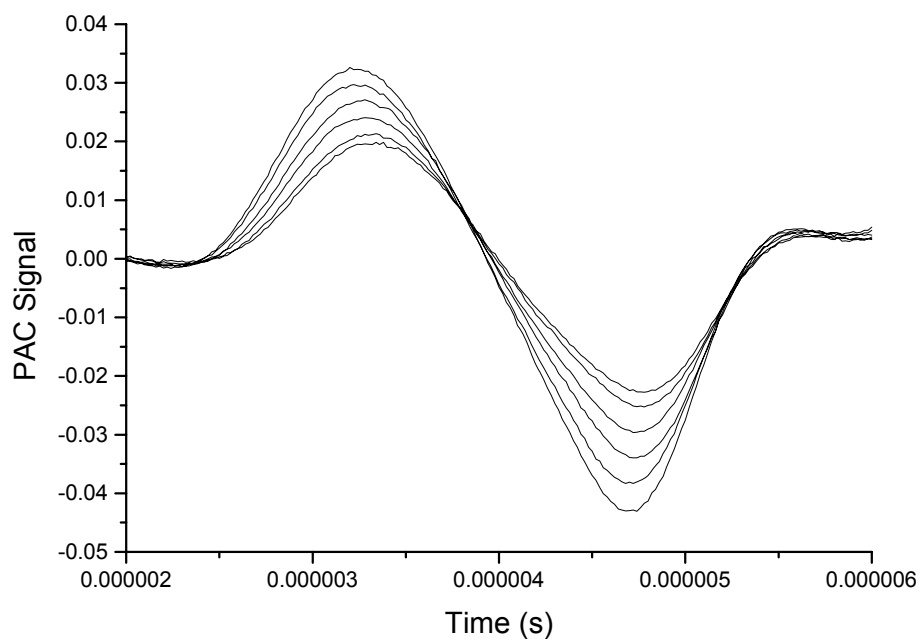
Figure 3.22: Overlay of the sample acoustic wave at temperatures: 14, 17, 20, 23, 26, and 29 ºC, for CO photodissociation from CO-LPO in 100mM Tris-HCl (pH=7.0)
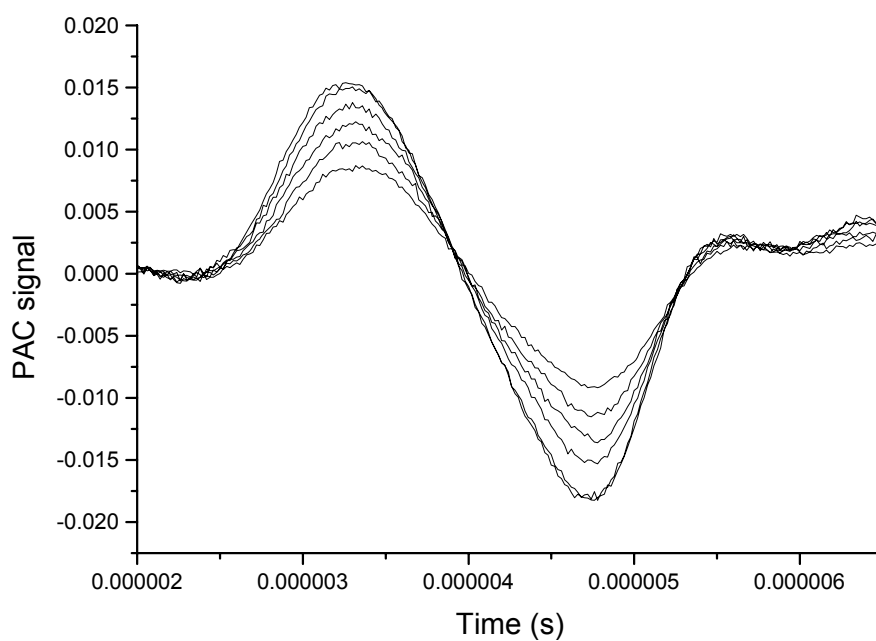


Figure 3.23: Overlay of the reference acoustic wave at temperatures: 14, 17, 20, 23, 26, and 29 ºC, for the heat release from 4sp to solution, in 100mM Tris-HCl (pH=7.0)

At pH=7.0, the volume and enthalpy changes were measured in both 100 mM Tris-HCl and 100 mM sodium phosphate buffer to investigate the possibility that the volume and enthalpy changes observed were due to proton release/uptake associated with the photodissociation from CO-LPO. The volume change due to protonation of Tris is negligible while protonation of sodium phosphate buffer contributes to a volume increase of 20 ml·mol$^{-1}$. The change in enthalpy of protonation of the sodium phosphate buffer is minimal compared to that of protonation of the Tris buffer, as well. The overlay of the sample and reference acoustic waves, determined under other conditions, showed the same pattern (no phase shift between).

The sample/reference acoustic wave overlay for CO photodissociation from CO-LPO in 50 mM acetate buffer (pH=4.0) and 100 mM CAPS buffer (pH=10.0) are shown in Figure 3.24 and 3.25, respectively.
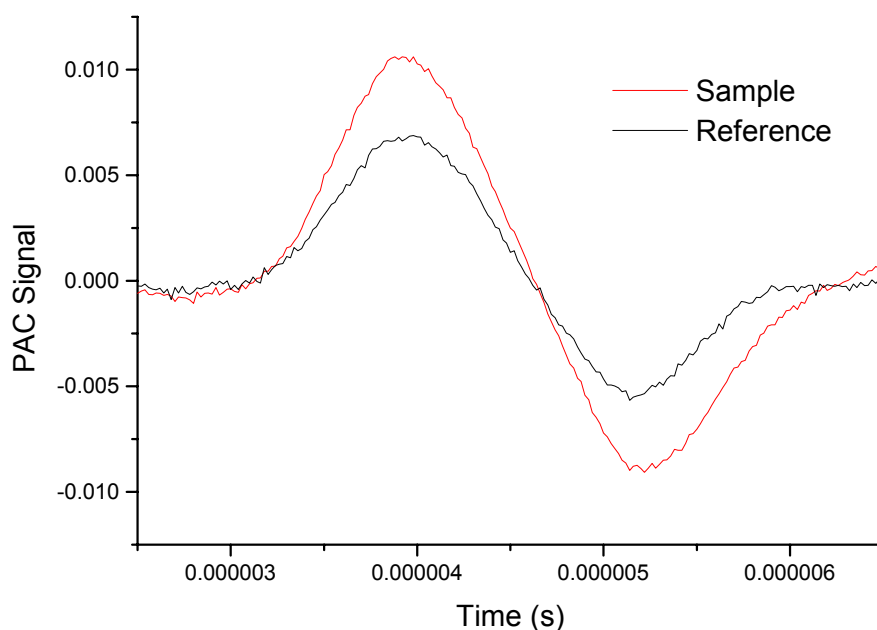


Figure 3.24: Overlay sample and reference waves for photodissociation of from CO-LPO in 50 mM acetate buffer (pH=4.0), 23 ºC.
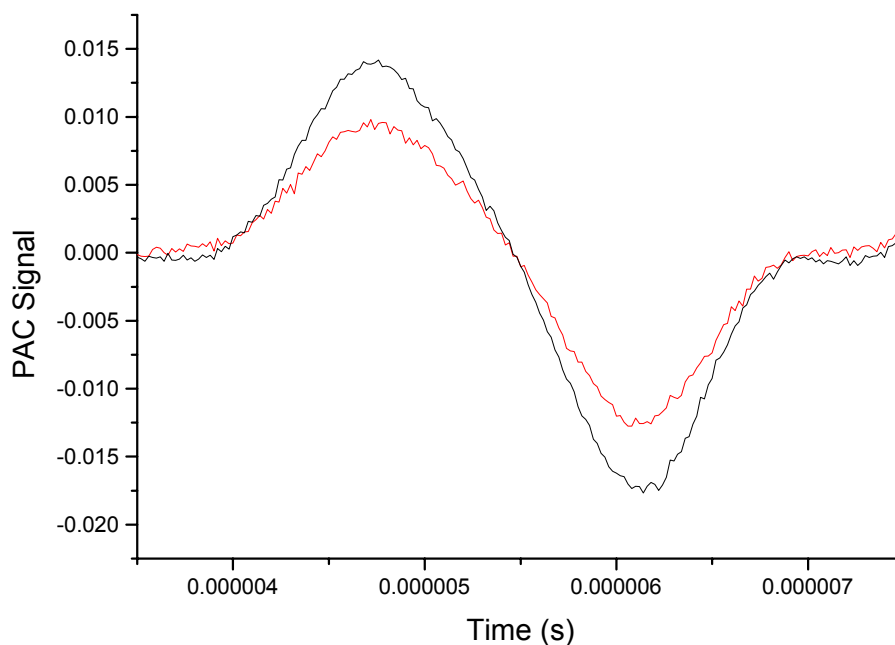
Figure 3.25: Overlay of the sample and reference acoustic waves for photodissociation of CO-LPO in 100 mM CAPS buffer (pH=10.0), 23 ºC.

In order to extrapolate the volume and enthalpy of photodissociation of CO from CO-LPO, the ratio of the amplitude of the sample and reference signal, multiplied by the energy of the laser ($E_{h\nu}$), was plotted as a function of $C_p\rho/\beta$ according to Equation 11. Plots for CO-LPO in 50 mM acetate buffer (pH=4.0), 100 mM Tris-HCl (pH=7.0), 100 mM sodium phosphate buffer (pH=7.0), and 100 mM CAPS buffer (pH=10.0) are shown in Figure 3.26. The volume and enthalpy changes for the reaction volume and enthalpy changes at pH=4.0, 7.0, and 10.0 in Table 3.3.
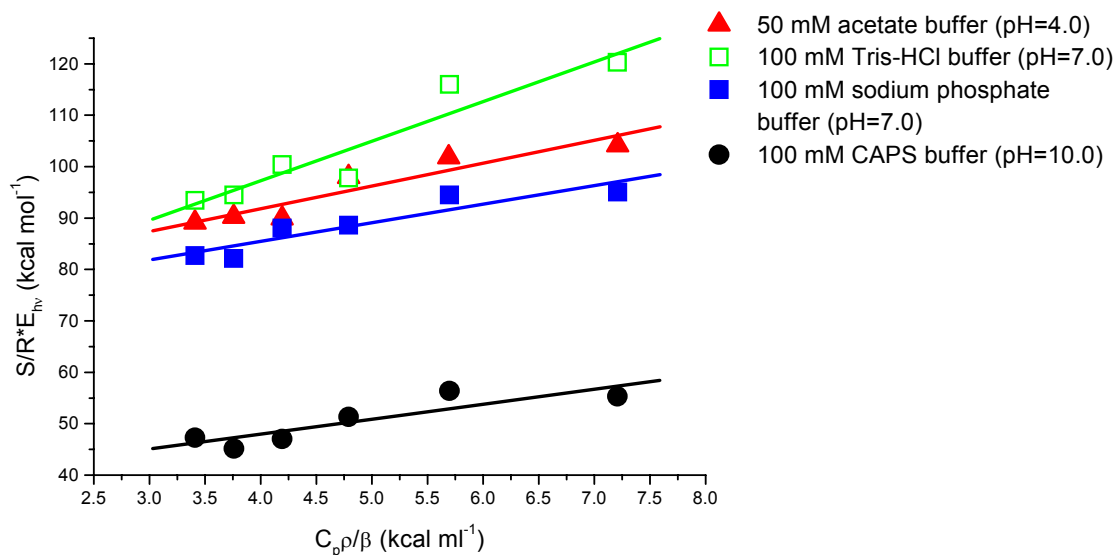
Figure 3.26: Plot of (S/R)*$E_{h\nu}$ versus Cp$\rho$/$\beta$ photodissociation of CO-LPO in 50 mM acetate buffer (pH=4.0), red triangle; 100 mM sodium phosphate buffer (pH=7.0), blue square; 100 mM Tris-HCl buffer (pH=7.0), open green square; 100 mM CAPS buffer (pH=10.0), black circle.

Table 3.3 Thermodynamic parameters for photolysis of CO-LPO at pH=4.0, 7.0, 10.0 and in 100 mM Tris-HCl/100 mM, 250 mM, and 500 mM NaCl (pH=7.0).

| Buffer | $\Delta H$ (kcal·mol$^{-1}$) | $\Delta V$ (ml·mol$^{-1}$) |
|---|---|---|
| 50 mM acetate (pH=4) | -16.7 ± 7.3 | 1.9 ± 1.1 |
| 100 mM Tris-HCl (pH=7.0) | -20.1 ± 6.3 | 4.0 ± 1.3 |
| 100 mM sodium phosphate (pH=7.0) | -23.3 ± 6.1 | 3.6 ± 1.3 |
| 100 mM CAPS (pH=10.0) | 27.6 ± 4.5 | 6.0 ± 1.3 |
| 100 mM Tris-HCl/100mM NaCl (pH=7.0) | 8.8 ± 7.0 | 7.2 ± 1.0 |
| 100 mM Tris-HCl/250mM NaCl (pH=7.0) | 29.5 ± 8.7 | 8.4 ± 1.0 |
| 100 mM Tris-HCl/500mM NaCl (pH=7.0) | 30.7 ± 13.0 | 9.5 ± 2.4 |

The volume change of photodissociation of CO from CO-LPO at pH=4.0, 7.0, and 10.0 were much less than expected ~ 3.3 ml ·mol$^{-1}$. In order to identify the processes that contribute to the observed volume and enthalpy changes, the thermodynamic parameters associated with the ligand photorelease as a function of ionic concentration have been characterized. Values for $C_p\rho$/$\beta$ for buffers with higher ionic concentrations had to be

calculated. As the ionic strength was increased, the amplitude of the acoustic wave increased. The values of $C_p\rho/\beta$ for 100, 250, and 500 mM NaCl were determined at temperatures 14, 16, 18, 20, 22, 24, 26, and 32 ºC as described in the Material and Methods section, 2.5.3, using Equation 16. Figure 3.27 shows the calculated $C_p\rho/\beta$ values as a function of temperature.
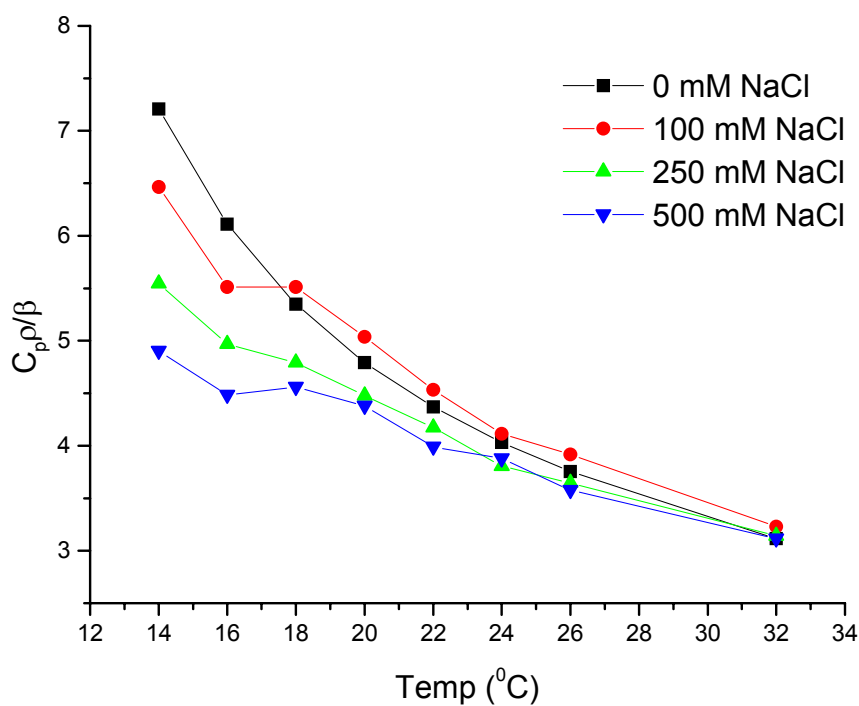


Figure 3.27 $C_p\rho/\beta$ as a function of temperature for 4sp in 100 mM Tris-HCl/0 mM NaCl (black), 100 mM NaCl (red), 250 mM NaCl (green), and 500 mM NaCl (blue).

The sample/reference acoustic wave overlay for photodissociation of CO from CO-LPO at 23 °C in 100 mM Tris-HCl/100 mM NaCl is shown in Figure 3.28. The sample acoustic wave is shown in red and the reference acoustic wave in black. The sample and reference acoustic waves were overlaid at temperatures 14, 17, 20, 23, 26, and 29 °C and the plots are shown in Figures 3.29 and 3.30, respectively.
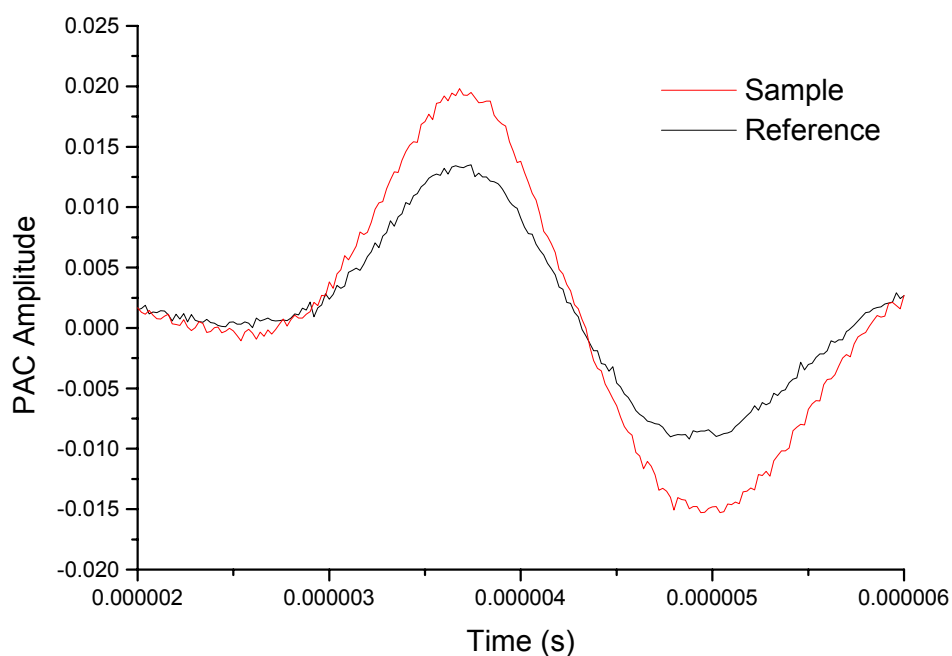


Figure 3.28: Sample (red) and reference (black) acoustic wave overlay at 23 °C for photodissociation of CO from CO-LPO in 100 mM Tris-HCl/100 mM NaCl (pH=7.0).
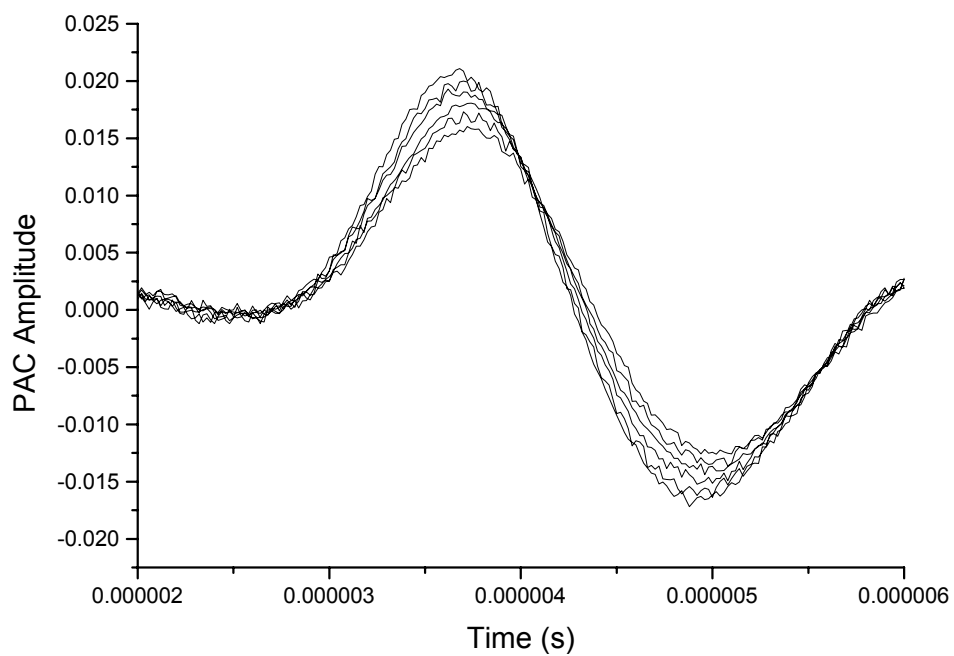
Figure 3.29: Sample acoustic waves overlaid at temperatures 14, 17, 20, 23, 26, and 29 °C for CO photodissociation from CO-LPO in 100 mM Tris-HCl/100 mM NaCl (pH=7.0).
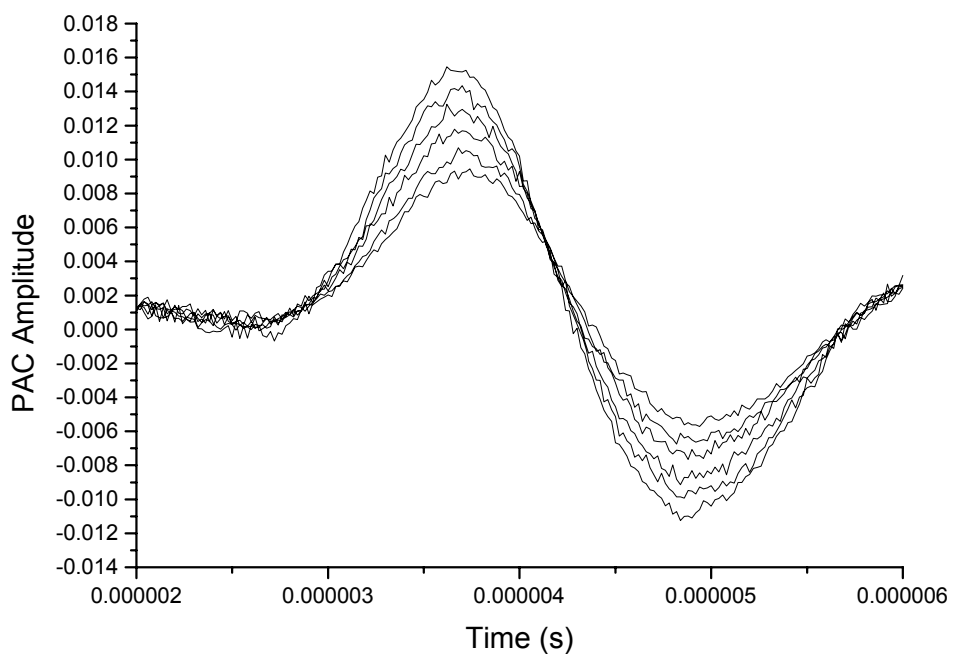


Figure 3.30: Reference acoustic waves overlaid at temperatures 14, 17, 20, 23, 26, mM Tris-HCl/100 mM NaCl (pH=7.0).

Inspection of the sample and reference wave overlay for CO photodissociation from CO-LPO at 23 ºC for 100 mM, 250 mM, and 500 mM NaCl revealed that there was no shift in phase, indicating that the volume and enthalpy changes occurred faster than 50 ns. The ratio of the sample and reference amplitudes, multiplied by the energy of the laser, were plotted versus $C_p\rho/\beta$ (according to equation 11), the plots are shown in Figure 3.31.
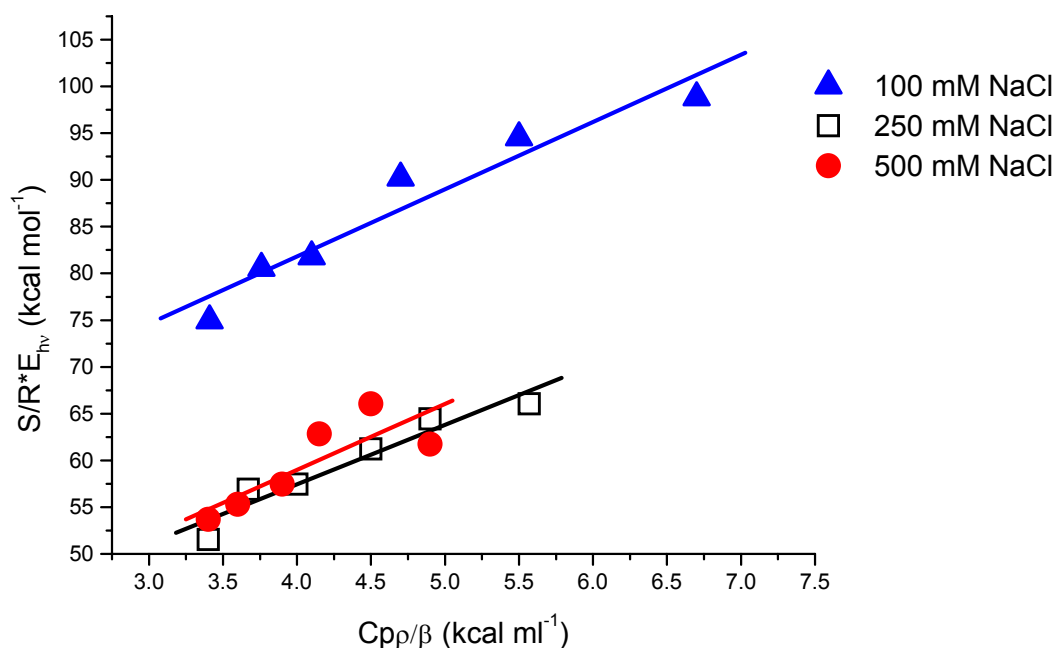


Figure 3.31: Plot of (S/R)*Ehν versus $Cp\rho/\beta$ photodissociation of CO-LPO in 100 mM Tris-HCl/10 0 mM NaCl buffer (pH=7.0), blue triangle; 100 mM Tris-HCl/250 mM NaCl buffer (pH=7.0), open black square; 100 mM Tris-HCl/500 mM NaCl buffer (pH=7.0), red circle.

The volume and enthalpy changes observed for the photorelease of CO from CO-LPO in 100 mM Tris-HCl/100 mM NaCl, 250 mM NaCl, and 500 mM NaCl are reported in Table 3.3. The volume change for photodissociation of CO from CO-LPO becomes larger at 250 mM NaCl and 500 mM, going from ~3 ml·mol$^{-1}$at 0 mM and 100 mM NaCl

ionic strength to ~9 ml·mol$^{-1}$ at 500 mM NaCl.  The enthalpy change at 100 mM, 250

mM, and 500 mM NaCl ionic concentrations were endothermic. At 250 mM NaCl and

500 mM NaCl, the change in enthalpy were similar to the endothermic values obtained

for CO photodissocaition from CO-LPO at pH=10.0, ≈20 kcal·mol$^{-1}$.

## 4.0 Thermodynamic profile for CO binding to LPO

Combining data obtained from PAC, TA, and the binding constant a thermodynamic profile ($\Delta G$, $\Delta H$, and $\Delta S$) for CO binding to $Fe^{(II)}LPO_{final}$ could be constructed. From the CO binding constant, the free energy of formation of the CO-LPO complex was determined to be $\Delta G = -7$ kcal·mol$^{-1}$ using Equation 11. Transient absorption results allowed for the characterization of the transition state for CO-LPO photolysis. PAC results gave the reaction volume and enthalpy changes. By using Equation 17 the reaction enthalpy for CO binding can be determined.

$$\Delta H = \Delta H^{\neq}_F - \Delta H^{\neq}_B \qquad\qquad (17)$$

Where $\Delta H^{\neq}_F$ is the activation enthalpy for the forward reaction, and $\Delta H^{\neq}_B$ is the activation enthalpy of the backward reaction. The entropy of photodissociation of CO from LPO was calculated using the following equation:

$$\Delta G = \Delta H - T\Delta S \qquad\qquad (18)$$

$\Delta G$ was determined from the binding constant of CO binding to LPO and T is the temperature (25ºC). From this data a thermodynamic profile for CO binding to LPO was constructed. Figure 4.1 shows the free energy thermodynamic profile for formation of the CO-LPO complex at pH=7.0, 25ºC. The enthalpy profile in Figure 4.2 shows that formation of the CO-LPO complex is endothermic. However, the entropy profile shown in Figure 4.3 illustrates that formation of the CO-LPO complex is entropically favorable. Using the value for activation volume published previously, -10ml·mol$^{-1}$ [41], the volume profile for the formation of the CO-LPO complex was constructed. The change in volume for formation of the CO-LPO complex is about -4 ml·mol$^{-1}$. The negative

volume change indicates that the rate limiting step in the reaction is the formation of the covalent bond between the Fe and CO.
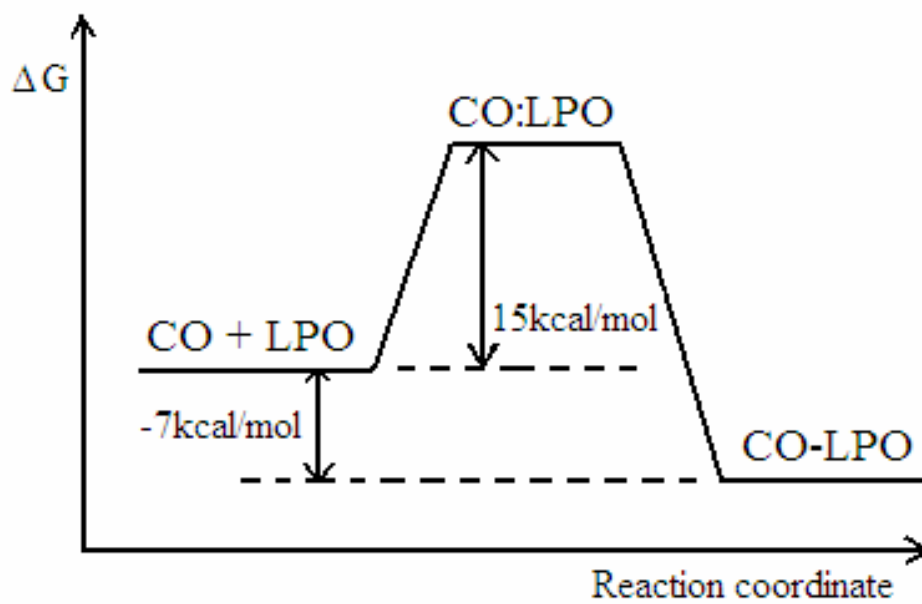


Figure 4.1: Free energy profile of CO binding to LPO
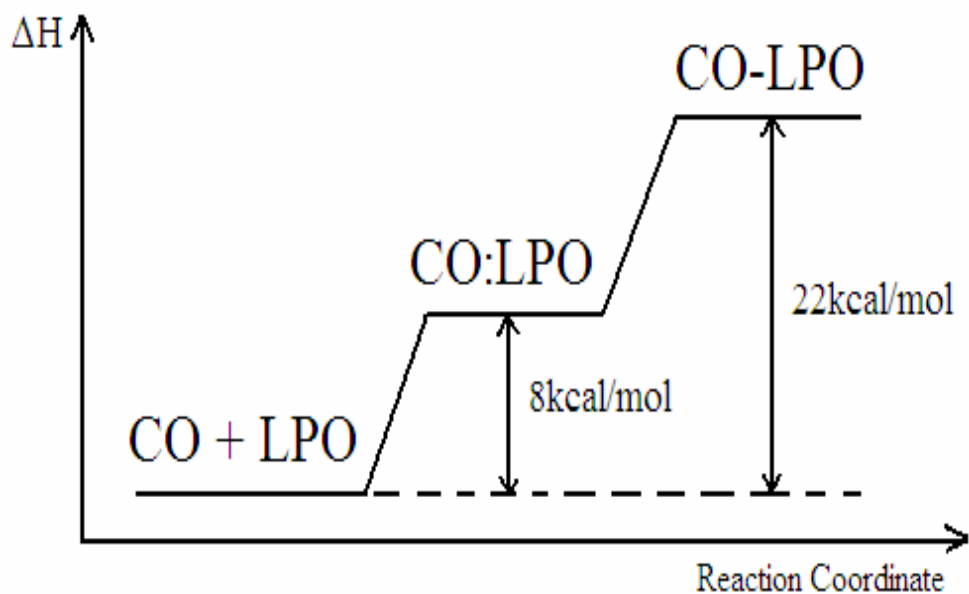
Figure 4.2: Enthalpy profile of CO binding to LPO
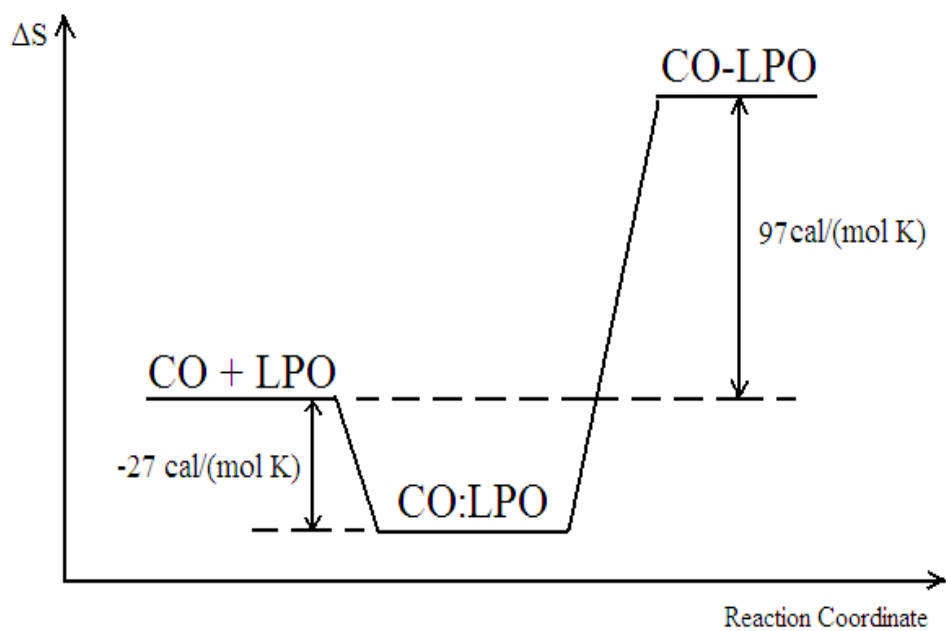


Figure 4.3: Entropy profile of CO binding to LPO
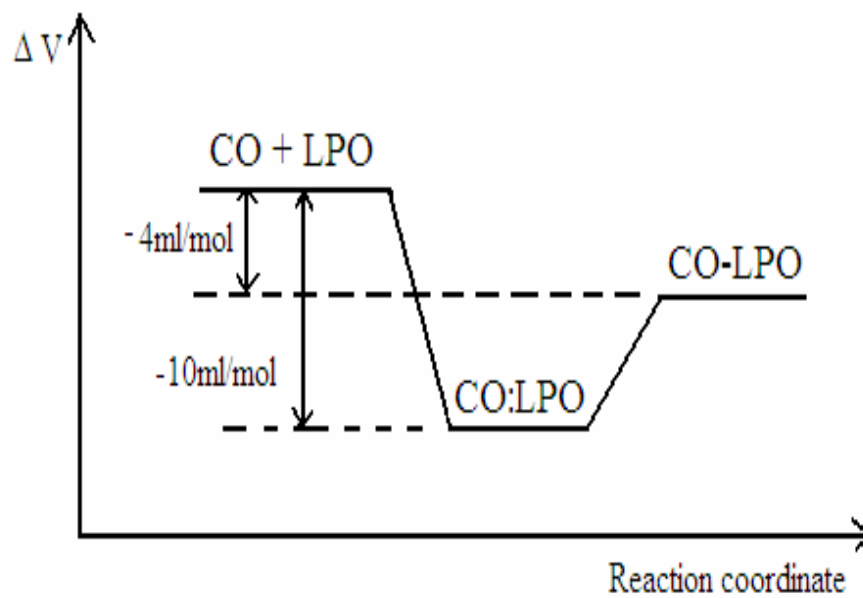
Figure 4.4: Volume profile of CO binding to LPO

## 5.0    Discussion

## 5.1    UV-visible spectroscopy discussion

These data show that $Fe^{(III)}LPO$ has a Soret maximum at 412 nm and four visible bands at 501, 542, 585, and 638 nm and these results are in accord with previously published results [35].   Following reduction with sodium dithionite, $Fe^{(III)}LPO$ is converted initially to $Fe^{(II)}LPO_{intermediate}$ with a rate constant of $1.3x10^5$ $M^{-1} \cdot s^{-1}$ [42,43]. The initial conformation of $Fe^{(II)}LPO_{intermediate}$ exhibits a Soret maximum at 447 nm and visible bands at 532, 563, and 598 nm. The broad Soret maximum at 433 nm of the $Fe^{(II)}LPO_{final}$ state indicates that there are two conformations in equilibrium. The two conformations are believed to have either an open active site or a constrained active site [30]. The $Fe^{(II)}LPO_{intermediate}$ at acidic pH was not observed. It is likely that the transition from the intermediate to the final reduced state occurs faster than the resolution of our instrument.  However, we cannot exclude that the intermediate state is not populated at acidic pH. The conformation of $Fe^{(II)}LPO_{final}$ at pH=4.0 exhibits a Soret maximum of 433 nm.  The $Fe^{(II)}LPO_{final}$ conformation at pH=4.0 is not very stable and appeared to become easily oxidized.   Early studies claim that the conformation of $Fe^{(II)}LPO_{final}$ is really another intermediate of reduced, which then assumes another conformation with an absorption spectra identical to the original $Fe^{(III)}LPO$ absorption spectra [31]. To better understand the factors that influence the stability of the $Fe^{(II)}LPO_{intermediate}$, the rate of conversion of $Fe^{(II)}LPO_{intermediate}$ to $Fe^{(II)}LPO_{final}$ in the range from pH=7.0 to pH=11.0 was measured.   Measurement of the rate of conversion of $Fe^{(II)}LPO_{intermediate}$ to $Fe^{(II)}LPO_{final}$ revealed that the transition is a pH dependent biphasic process. The lifetimes of the $Fe^{(II)}LPO_{intermediate}$ conversion to $Fe^{(II)}LPO_{final}$ are not pH dependent but, the percent

amplitudes of the fast and slow phases show a significant pH dependence. The percent amplitudes of the fast and slow phases were plotted as a function of pH (Figure 3.12). The data were then fit using the Henderson-Hasselbalch equation, that provided the $pK_a$ for the fast and slow phases to be 9.1 and 9.3, respectively. The fast and slow phase $pK_a$ were averaged giving a $pK_a$ of 9.2. The $pK_a$ of the fits indicates that the conformational change of $Fe^{(II)}LPO_{intermediate}$ to $Fe^{(II)}LPO_{final}$ is strongly influenced by the protonation state of a residue or cluster of residues with a $pK_a$ close to 9.2.

Taking into account the $pK_a$ value 9.2, the possible amino acid residues that can influence the conversion of the $Fe^{(II)}LPO_{intermediate}$ to $Fe^{(II)}LPO_{final}$ are arginine and/or lysine. Arg372 is the residue closest to the heme and is likely to influence the pathway of the transition of $Fe^{(II)}LPO_{intermediate}$ to $Fe^{(II)}LPO_{final}$. At pH above 9.2, $Fe^{(II)}LPO$ with the deprotonated state of Arg372 becomes populated and the slow conversion pathway is dominant. When the pH is between 7.0 and 9.2 the Arg372 becomes protonated and the fast conversion pathway of $Fe^{(II)}LPO$ to its final conformation becomes more facile. At pH less than 7.0, the $N_\varepsilon$ on the imidazole ring of His226, which is located in the heme-binding pocket, will become protonated. We speculate that the protonation of His226 accelerates $Fe^{(II)}LPO_{intermediate}$ conversion at acidic pH and the kinetics of this reaction cannot be resolved by our instrument.

## 5.2    Transient absorption spectroscopy discussion

Previous studies on ligand binding to $Fe^{(II)}$LPO have elucidated several aspects about the active site of LPO.  Abu-Soud *et al* [35] have analyzed CO binding to $Fe^{(II)}$LPO using stopped-flow technique. They reported that ligand binding is a biphasic process with a fast phase rate constant of $1.40 \times 10^3$ $M^{-1} \cdot s^{-1}$ and a slow phase rate constant of $0.59 \times 10^3$ $M^{-1} \cdot s^{-1}$ [35]. From these results and results from steady state absorption spectroscopy, the authors have proposed that reduced LPO has two conformations, one with an open active site and one with a more constrained active site [35].

However, in contrast to the above results, other studies have reported that CO binding to the active site of $Fe^{(II)}$LPO is a monophasic process and is gated by conserved residues located in the distal heme pocket [24].  Ciaccio *et al* [24] performed kinetic measurements of CO binding to $Fe^{(II)}$LPO as a function of pH.  From the stopped flow analysis of CO binding to LPO at pH=7.0, a monophasic bimolecular rate constant of $2.5 \times 10^4$ $M^{-1} \cdot s^{-1}$ at 25 ºC, was reported.  A similar rate constant ($k=2.75 \times 10^4$ $M^{-1} \cdot s^{-1}$) was reported for CO rebinding to LPO subsequent to laser photolysis, recorded at pH=7.0 and 25ºC [30]. From the analysis of the pH dependence of the rate of CO binding to LPO, two amino acid residues (Arg372 and His226) were identified to be involved in gating the reaction [24].  From a cyclic voltametry study, the same residues were proposed to control the redox potential of LPO [24].

Here we report our results on the characterization of CO rebinding to $Fe^{(II)}$LPO at pH=4.0,  7.0,  and  10.0  as  a  function  of  temperature,  using  transient  absorption spectroscopy. Subsequent to photolysis of CO-LPO, the geminate pair (CO:LPO) is formed, where CO resides in the heme pocket but is not ligated to the heme.

Subsequently CO will either quickly rebind to the heme or CO will leave the protein.  In the case of lactoperoxidase CO leaves the protein with $\Phi$=0.75 [24].  Our results show that CO rebinding to $Fe^{(II)}$LPO was a monophasic process with k= $2.7 \times 10^4 \ M^{-1} \cdot s^{-1}$ and $4.9 \times 10^4 \ M^{-1} \cdot s^{-1}$ at 23 ºC, at pH=4.0 and 7.0, respectively.  When the pH was raised to 10.0 the rate of CO rebinding to $Fe^{(II)}$LPO was biphasic and the rate constant for the fast and slow phases were k=$7.1 \times 10^4 \ M^{-1} \cdot s^{-1}$ and $1.3 \times 10^4 \ M^{-1} \cdot s^{-1}$, respectively.

These results show that the rate of CO binding to $Fe^{(II)}$LPO is pH dependent, in agreement with reports from Ciaccio *et al* [24].  However, Ciaccio *et al* reported an order of magnitude increase in rate of reaction from acidic to neutral pH, and then an additional order of magnitude increase when the pH was increased to 10 [24].  The results from our study do not show such significant pH dependence with the rate constant at 23ºC increasing by two times when the pH was increased from 4.0 to 7.0.  The rate constant increased by three times when the pH was increased to 10.0.  The discrepancies between the results of our study and other studies are not clear.  The purity and source of the protein may contribute the different values of the rate constant.

The traces of CO rebinding to $Fe^{(II)}$LPO were collected as a function of temperature to elucidate the activation enthalpy and entropy. The activation enthalpy and entropy attained from an Eyring plot for pH 4.0, 7.0, and 10.0 were, within error, very similar, except for the slow phase at pH=10.0.   The slow phase activation enthalpy and entropy were $3.8 \pm 1.7$ kcal·mol$^{-1}$ and $-39.8 \pm 5.8$ cal·mol$^{-1}$·K$^{-1}$, respectively.  The slow phase process has a lower activation enthalpy than the fast phase process at pH=4.0 and 7.0 but has a greater decrease in entropy.  The significant decrease in activation entropy indicates that there is a large conformational rearrangement of the LPO active site.

## 5.3 Photoacoustic calorimetry discussion

We have employed photoacoustic calorimetry to determine the volume and enthalpy changes associated with photodissociation of CO from CO-LPO. The lack of phase shift of the sample wave compared to that of the reference wave, indicates that the ligand migration through the protein to solvent and the respective volume and enthalpy changes are occurring faster than 50 ns. Several processes occur upon photodissociation of CO from heme center, including breaking of the CO-LPO bond, transition of the heme from low-spin to high-spin, migration through the active site, and then migration through the protein into solution. These processes are often associated with protein conformational changes, electrostriction, proton release/uptake. All these processes are also associated with volume and enthalpy changes.

The enthalpy of the reaction can be written in equation form as:

$$\Delta H_{total} = \Delta H_{Fe-CO} + \Delta H_{LS-HS} + \Delta H_{CO\ Solvation} + \Delta H_{conformational} \qquad (19)$$

The values for $\Delta H_{Fe-CO}$, $\Delta H_{LS-HS}$, and $\Delta H_{CO\ Solvation}$ have been determined previously from other heme proteins and heme model compounds. The Fe-CO bond has been calculated elsewhere to be ~15-17 kcal·mol$^{-1}$ [44], $\Delta H_{LS-HS}$ is less than 1 kcal·mol$^{-1}$ [39], and solvation of CO is ~5 kcal·mol$^{-1}$ [39]. The predicted enthalpy change for photodissociation should be endothermic and close to ~20 kcal·mol$^{-1}$ [39]. Any additional processes that may occur during the reaction are accounted for in the $\Delta H_{conformational}$ term. At pH=4.0 and 7.0 the observed reaction $\Delta H$ ~ -20 kcal·mol$^{-1}$ suggests that an exothermic process of ~-40 kcal·mol$^{-1}$ must occur to overcome the enthalpy of breaking of the Fe-CO bond and solvation of CO. The change in volume for pH=4.0 and 7.0 were about ~3 ml·mol$^{-1}$. Photodissociation of CO from LPO was

performed in both 100 mM sodium phosphate buffer and 100 mM Tris-HCl at pH=7.0 to determine if the proton release/uptake is associated with ligand dissociation. Protonation of the Tris-HCl buffer is associated with the volume change of -1 ml·mol$^{-1}$; in contrast, protonation of the sodium phosphate buffer is associated with a volume increase of 24 ml·mol$^{-1}$ [45]. The similar values of volume change determined in both buffers confirm that proton release/uptake does not occur during ligand photolysis. When the pH was raised to 10.0, $\Delta H$ became endothermic (27.6 ± 4.5 kcal·mol$^{-1}$), in agreement with the predicted enthalpy for CO-Fe bond cleavage.

The change in volume due to photodissociation of CO from Fe$^{(II)}$LPO can be written as the sum of the individual contributions:

$$\Delta V_{total} = \Delta V_{Fe\text{-}CO} + \Delta V_{LS\text{-}HS} + \Delta V_{CO\,Solvation} + \Delta V_{conformational} \qquad (20)$$

The volume changes determined from photolysis of CO-Fe$^{(II)}$ heme model complexes show that breaking of the Fe-CO bond, $\Delta V_{Fe\text{-}CO}$, accounts for a volume increase of ~5 ml·mol$^{-1}$, $\Delta V_{LS\text{-}HS}$ is 8 ml·mol$^{-1}$, and $\Delta V_{CO\,Solvation}$ is ~17 ml·mol$^{-1}$ [39]. In the case of LPO, the heme is buried deep within the protein matrix and the protein may buffer the contribution of $\Delta V_{LS\text{-}HS}$ and $\Delta V_{Fe\text{-}CO}$ to the global volume change and $\Delta V_{total}$. In such a case, the major contribution to $\Delta V_{total}$ would originate from solvation of CO with $\Delta V_{total}$ ≈20 ml·mol$^{-1}$. Any additional processes that may occur are accounted for in the $\Delta V_{conformational}$ term. The observed volume changes for photolysis of CO-LPO in 50 mM acetate buffer (pH=4.0), 100mM Tris-HCl (pH=7.0), 100 mM sodium phosphate buffer (pH=7.0), and 100mM CAPS buffer (pH=10.0) were 1.4±1.1 ml·mol$^{-1}$, 5.2 ± 0.8 ml·mol$^{-1}$, 2.7 ± 1.0 ml·mol$^{-1}$, and 3.92 ± 2.7 ml·mol$^{-1}$, respectively.

Conformational changes associated with changes in charge distribution are likely to account for the small volume changes and exothermic enthalpy. Electrostriction of water molecules around solvated charges is exothermic and causes a volume decrease. To test the hypothesis that CO dissociation results in charge redistribution and the associated electrostriction, the reaction was examined at pH=7.0 in higher salt concentrations. The photodissociation of CO from $Fe^{(II)}$LPO could cause a rearrangement of charged residues that induce electrostriction. Under such conditions, ions are able to shield the exposed charges and in turn prevent electrostriction. When photolysis of CO-LPO was performed in 100 mM Tris-HCl/100 mM, 250 mM, and 500 mM NaCl (pH=7.0), an endothermic reaction, reflecting the dissociation of the CO-LPO bond and positive $\Delta V$ due to solvation of CO, should be observed. At increased NaCl concentrations a positive enthalpy change of ~30 ± 10 kcal·mol$^{-1}$ was observed, as expected for Fe-CO bond dissociation. The change in volume was two times greater at higher salt concentrations than at 0 mM ionic concentration buffers. The increase in reaction volume and enthalpy compared to those at 0 mM ionic concentration buffers indicates that electrostriction was contributing to the observed reaction volume and enthalpy changes at pH=7.0. The expected volume change of ~20 ml·mol$^{-1}$ was not seen fully because even at higher ionic concentration buffers all the exposed charges may not be entirely shielded.

Positive volume and enthalpy changes determined at higher salt concentrations were similar to be similar to that at pH=10.0. In 100 mM Tris-HCl/250 mM and 500 mM NaCl (pH=7.0) the respective changes in enthalpy were 29.5 ± 8.7 and 30.7 ± 13.0

kcal·mol$^{-1}$. The fact that electrostriction occurs at acidic and neutral pH but not at alkaline pH suggests that that residues with a pK$_a$ greater than 7.0 participates in the reaction.

Previous studies have shown that the photodissociation of CO from sperm whale myoglobin is often associated with breaking of a salt bridge between the propionate group of the porphyrin ring and arginine or lysine residue [46], due to doming of the protoporphyrin ring. The doming of the protoporphyrin ring results in the propionate group attached to the d-ring to move, and in turn disrupts a salt bridge. The model of the LPO structure in Figure 5.1 shows that Arg557 is in the vicinity and is in hydrogen bonding distance of the propionate group on the d-ring of the heme. It is likely that CO dissociation and subsequent displacement of the propionate group leads to the cleavage of this salt bridge. The structure of LPO in Figure 5.1 shows that there is a network of charged residues (Asp254, Glu233, Asp560, and Arg279) that can form a cluster of hydrogen bonds and salt bridges that connect Arg557 to the surface of the protein. Upon photolysis of CO-LPO the salt bridge between the propionate group and Arg557 is likely to be disturbed, causing a domino effect that rearranges the residue network including charge distribution. As a result, electrostriction occurs on the surface of the protein. On the other hand, at pH=10.0, the bridge between Arg557 and the propionate group is not formed, which results in different volume and enthalpy changes. The similar results observed for high salt concentrations confirm the electrostriction origin of the observed volume and enthalpy changes. Interestingly, in comparison to HRP, which does not have this salt bridge network, previous PAC studies report an enthalpy and volume change for photolysis of CO-LPO of $42 \pm 8$ kcal·mol$^{-1}$ and $20 \pm 1$ ml·mol$^{-1}$ [47]. This is very similar to our results at pH=10.0.
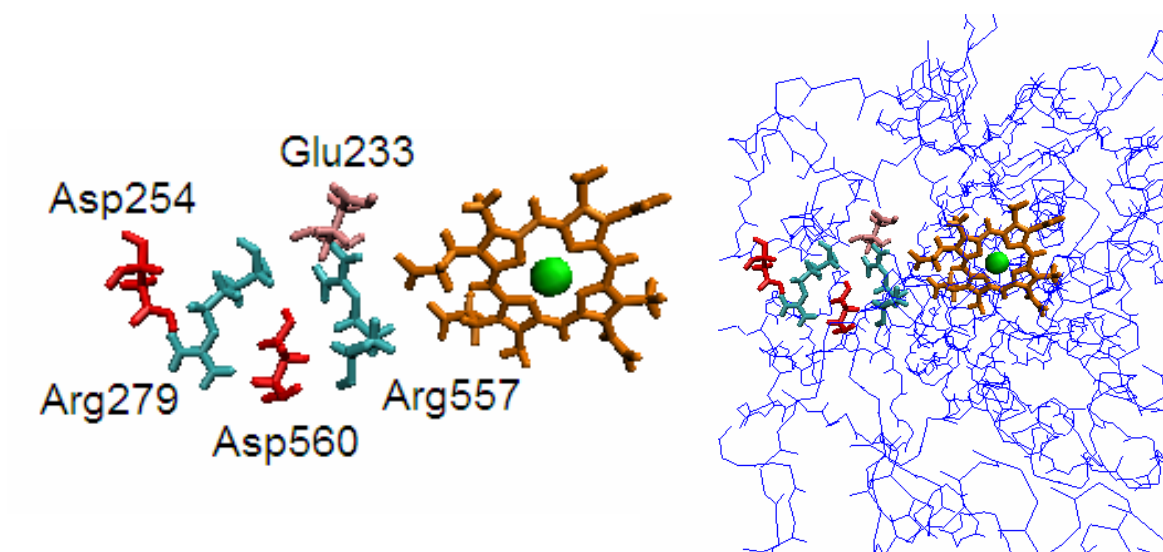
Figure 5.1: Model of the salt bridge of lactoperoxidase. On the left hand side is the heme and salt bridge/hydrogen-bonding network. The right hand image displays the salt bridge/hydrogen-bonding network from the active site to the surface of the protein.

## 6.0    Conclusion

For the first time the rate of conversion of $Fe^{(II)}LPO_{intermediate}$ conversion to $Fe^{(II)}LPO_{final}$ has been measured.  Results show that the protonation state of Arg372 may influence the pathway, fast or slow, at which this conversion occurs.   UV-visible spectroscopy results revealed that the binding constant of CO to $Fe^{(II)}LPO$ was about ten times less than that of myoglobin but is still on the order of heme proteins. From the binding constant the free energy of formation of the CO-LPO complex was determined.

Transient absorption results were used to characterize thermodynamic parameters of the transition state for CO binding to LPO.  The rate constant of CO rebinding to LPO is about 10 times less than the rate constant for myoglobin and indicates that the access channel to the active site is narrow, and has been reported elsewhere. The increase of the rate constant of CO rebinding to LPO as pH was increased indicated that at higher pH the active site of LPO is more open, reported previously.   CO rebinding is biphasic at pH=10.0, but due to error and without further research, we can not determine why this is seen.

Photoacoustic calorimetry was used to determine the thermodynamic parameters of CO photodissociation from LPO.  The results indicate that the photoinitiated reaction is associated with the cleavage of a salt bridge between the propionate side chain of the porphyrin d-ring and Arg557.  Disruption of the salt bridge results in a cascade effect that disrupts a network of residues that participate in a hydrogen bonding/salt bridge network to the surface of the protein, resulting in electrostriction on the surface of the protein.

From the results of CO binding and photodissociation of CO from LPO, at pH=7.0, we were able to construct a thermodynamic profile of CO binding to LPO.  The

thermodynamic profile shows that CO binding to LPO is endothermic but is an entropy driven reaction.  The salt bridge and hydrogen-bonding network that connects the active site to the surface of the protein may help modulate substrate binding and recognition.

# Appendix A

| Chemical | Company |
| --- | --- |
| 4sp, Fe$^{(III)}$meso-tetra(4-sulfonatophenyl)porphyrin chloride | Frontier Scientific |
| Acetic acid, glacial | Fisher-Scientific |
| Acrylamide | Fisher-Scientific |
| Ammonium Persulfate C | Fisher-Biotech |
| Bis-Acrylamide | Fisher-Biotech |
| Brilliant Blue R-250 | Fisher-Biotech |
| CAPS, N-Cyclohexyl-3-aminopropanesulfonic acid | Sigma-Aldrich |
| CM-52, Carboxy Methylcellulose | Whatman |
| Dalton - Mark (VII) SDS-7 | Sigma-Aldrich |
| HCl, reagent grade | Fisher-Scientific |
| Lactoperoxidase | Sigma-Aldrich |
| Lactoperoxidase | Worthington |
| NaCl | Fisher-Scientific |
| NaOH, reagent grade | Fisher-Scientific |
| pH Buffers 4.0, 7.0, 10.0 | Fisher-Scientific |
| SDS, electrophoresis grade | Fisher-Biotech |
| Sodium acetate | Fisher-Scientific |
| Sodium dithionite | Fluka or Fisher-Scientific |
| Sodium phosphate, dibasic anhydrous | Fisher-Scientific |
| Sodium phosphate, monobasic | Fisher-Scientific |
| Temed, N,N,N',N'-Tetramethylethylenediamine | Fisher-Biotech |
| Tris hydroxymethyl aminomethane hydrochloride | Fisher-Biotech |
| Vacuum Grease | VWR |

## Appendix B

| Electrophoresis Solutions and Gels | |
|---|---|
| **Stock Solutions** | **Chemical** |
| 10% ammonium persulfate c | • 0.1g adjusted to 1ml |
| 30% acrylamide/0.8% bisacrylamide | • 6.0g acrylamide<br>• 0.16 N,N'-methylene-bisacrylamide<br>• 20ml $H_2O$<br>• Stored at 4ºC protected from sunlight |
| 4X Tris-Cl/SDS pH 8.8 | • 182g Tris base<br>• 600ml $H_2O$<br>• pH adjusted to 8.8 with 1M HCl<br>• 1000ml $H_2O$<br>• 4g electrophoresis-grade SDS<br>• Store at 4ºC |
| 4X Tris-Cl/SDS pH 6.8 | • 12.1g Tris base<br>• 80ml $H_2O$<br>• pH adjusted to 6.8 with 1M HCl<br>• Adjust volume to 200ml with $dH_2O$<br>• 0.8g electrophoresis-grade SDS<br>• Store at 4ºC |
| 1X SDS/electrophoresis buffer | • 15.1g Tris base<br>• 72.0g glycine<br>• 5.0g SDS<br>• 1000ml $H_2O$<br>• pH=8.3<br>• Store at 4ºC<br>• For use, dilute 1:1 |
| De-staining solution | • 25% methanol<br>• 65% $H_2O$<br>• 10% acetic acid |
| Sample buffer | • 125mM Tris-HCl pH6.8<br>• 10% 2-mercaptoethanol<br>• 10% SDS<br>• 10% glycerol<br>• bromophenol blue |
| Staining solution | • 0.2%Brilliant-Blue R250<br>• 45% methanol<br>• 45% water<br>• 10% acetic acid |

| Polyacrylamide Gels | |
|---|---|
| **Gel** | • **Solutions needed** |
| 7.5% separating gel | • 3.75ml 30% acrylamide/0.8% bisacrylamide<br>• 3.75ml 4X Tris-Cl/SDS, pH 8.8<br>• 0.10 ml 10% ammonium persulfate c<br>• 0.01 ml TEMED |
| 10% separating gel | • 5.0ml 30% acrylamide/0.8% bisacrylamide<br>• 4X Tris-Cl/SDS, pH=8.8<br>• 6.25ml $H_2O$<br>• 0.05ml ammonium persulfate c<br>• 0.1 TEMED |
| Stacking gel | • 0.65ml 30% acrylamide/0.8% bisacrylamide<br>• 1.25ml 4X Tris-Cl/SDS, pH 6.8<br>• .25 ml 10% ammonium persulfate c<br>• 0.01 ml TEMED |

## 7.0    References

1.  Enzymatic Catalysis. *Fundamentals of Biochemistry Life at the Molecular Level.* Voet, D., Voet, J., and Pratt, C. Eds.; John Wiley and Sons: New York, 2006; pp317-325.

2.  Introduction. Historical Background. *Heme Peroxidases*. Dunford, B. H., Ed.; John Wiley and Sons: New York; pp1-29.

3.  Terry, M. J., Linley, P. J., and Kohchi, T.  Making Light of It: The Role of Plant Haem Oxygenases in Phytochrome Chromophore Synthesis. *Biochem. Soc. Trans.* 2002, 30, 604-609.

4.  Jain, R. and Chan, M. Mechanism of Ligand Discrimination by Heme Proteins. *J. Biol. Inorg. Chem.* 2003, 8, 1-11.

5.  Spalteholz, H., Panasenko, O. M. and Arnhold, J. Formation of Reactive Halide Species by Myeloperoxidase and Eosinophil Peroxidase. *Arch. Biochem. Biophys.* 2006, 445, 225-234.

6.  Furtmuller, P.G., Zederbaur, M., Jantschko, W., Helm, J., Bogner, M., Jakopitsch, C., and Obinger, C. Active Site Structure and Catalytic Mechanism of Human Peroxidases. *Arch. Biochem. Biophys.* 2005, 445, 199-213.

7.  Ueda, T., Sakamaki, K., Kuroki, T., Yano, I., and Nagata, S. Molecular Cloning and Characterization of Human Lactoperoxidase. *Eur. J. Biochem.* 1997, 243, 32-4

8.  Laberge, M., Huang, Q., Schweitzer-Stenner, R. and Fidy, J. The Endogenous Calcium Ions of Horseradish Peroxidase C are Required to Maintain the Functional Nonplanarity of the Heme. *Biophys. J.* 2003, 84, 2542-2552.

9. De Gioia, L., Ghibaudi, E.M., Laurenti, E., Salmona, M. and Ferrari, R.P., A Theoretical Three-Dimensional Model for Lactoperoxidase, Built on the Scaffold of the Myeloperoxidase X-ray Structure. *J. Biol. Inorg. Chem.* 1996, 1, 476-485.

10. Obinger, C. Chemistry and Biology of Human Peroxidases. *Arch. Biochem. Biophys.* 2006, 445, 197-198.

11. Paul, K. and Ohlson, P. The Chemical Structure of Lactoperoxidase. *The Lactoperoxidase System; Chemistry and Biological Significance.* Pruitt, K. and Tenovuo, J, Eds. ; Marcel Dekker: New York, 1985; pp15-29.

12. Tenovuo, J., Lehtonen, O.J., Aaltonen, A.S., Vilja, P., and Tuohimaa, P. Antimicrobial Factors in Whole Saliva of Human Infants. *Infect. Immun.* 1986, 49-53.

13. Tenovuo, J. Clinical Applications of Antimicrobial Host Proteins Lactoperoxidase, Lysozyme and Lactoferrin in Xerostomia: Efficacy and Safety. *Oral Dis.* 2002, 8, 23-29.

14. Gorlewska, K.M., Teitel, C.H., Lay, J.O., Roberts, D.W., and Kadubar, F.F. Lactoperoxidase-catalyzed Activation of Carcinogenic Aromatic and Heterocyclic Amines. *Chem. Res. Toxicol.* 2004, 17, 1659-1666.

15. Ferrari, R.P., Travesa, S., De Gioia, L., Piercarlo, F., Suriano, G., and Ghibaudi, E.M. Catechol(amine)s as Probes of Lactoperoxidase Catalytic Site Structure: Spectroscopic and Modeling Studies. *J. Biol. Inorg. Chem.* 1999, 4, 12-20.

16. Odzemir, H., Uguz, M.T. In Vitro Effects of Some Anaesthetic Drugs on Lactoperoxidase. *J. Enzyme Inhib. Med. Chem.* 2005, 20, 491-495.

17. Morrison, M, Hultquist, and D.E. Lactoperoxidase II. Isolation. *J. Biol. Chem.* 1963, 238, 2847-2849.

18. Kumar, R. and Bhatia, K.L. Purification and X-ray Crystallographic Analysis of Lactoperoxidase from Buffalo Milk. *Acta. Cryst.* 1995, D51, 1094-1096.

19. Cals, M., Mailliart, P., Brignon, G., Anglade, P., and Dumas, B.R. Primary structure of Bovine Lactoperoxidase, a Fourth Member of a Mammalian Heme Peroxidase Family. *Eur. J. Biochem.* 1991, 198, 733-739.

20. Ghibaudi, E., Laurenti, E., Pacchiardo, C., Suriano, G., Moguilevsky, N., and Ferrari, R.P. Organic and Inorganic Substrates as Probes For Comparing Native Bovine Lactoperoxidase and Recombinant Human Myeloperoxidase. *J. Inorg. Biochem.* 2003, 94, 146-154.

21. Shin, K., Hayasawa, H., and Lonnerdal, B. Mutations Affecting the Calcium Binding Site of Myeloperoxidase and Lactoperoxidase. *Biochem. Biophys. Res. Commun.* 2001, 281, 1024-1029.

22. Sharique, M.S., Deva, W., and Behere, D. Fluoresence and Circular Dichroism Spectroscopic Studies on Bovine Lactoperoxidase. *BioMetals.* 1999, 12, 219-225.

23. Andersson, L.A., Bylkas, S.A., and Wilson, A.E. Spectral Analysis of Lactoperoxidase. *J. Biol. Chem.* 1996, 271, 3406-3412.

24. Ciaccio, C., De Sanctis, G., Marini, S., Sinibaldi, F., Santuccu, R., Arcovita, A., Bellelli, A., Ghibaudi, E., Rosa, P. F., and Coletta, M. Proton Linkage for CO Binding and Redox Properties of Bovine Lactoperoxidase. *Biophys. J.* 2004, 86, 448-454.

25. Zelent, B., Yano, T., Ohlsson, P.-I., Smith, M.L., Paul, J., and Vanderkooi, J.M. Optical Spectra of Lactoperoxidase as a Function of Solvent. *Biochemistry.* 2005, 44, 15953-15959.

26. Colas, C., Kuo, J.M., and Ortiz de Montellano, P.R. Asp-225 and Glu-375 in Autocatalytic Attachment of the Prosthetic Heme Group of Lactoperoxidase. J. Biol. Chem. 2002, 277, 7191-7200.

27. Wojciechowski, G., Huang, L., and Oritz de Montellano, P.R. Autocatalytic Modification of the Prosthetic Heme of Horseradish but not Lactoperoxidase by Thiocyanate Oxidation Products. A Role for Heme-Protein Covalent Cross-Linking. J. Am. Chem. Soc. 2005, 127, 15871-15879.

28. Hu, S., Treat, R.W., and Kincaid, J. R. Distinct Heme Active-Site Structure in Lactoperoxidase Revealed by Resonance Raman Spectroscopy. *Biochemistry*. 1993, 32, 10125-10130.

29. Thomas, E.L. Products of Lactoperoxidase-Catalyzed Oxidation of Thiocyanate and Halides. *The Lactoperoxidase System; Chemistry and Biological Significance*. Pruitt, K. and Tenovuo, J., Eds.; Marcel Dekker: New York, 1985; pp31-53.

30. Jantschko, W., Furtmuller, P.G., Zederbaur, M., Neugschwandtner, K., Jakopitsch, C., and Obinger, C. Reaction of Ferrous Lactoperoxidase with Hydrogen Peroxide and Dioxygen: An Anaerobic Stopped-flow Study. *Arch. Biochem. Biophys.* 2005, 434, 51-59.

31. Monzani, E., Gatti, A.L., Profumo, A., Casella, L., and Gullotti, M. Oxidation of Phenolic Compounds by Lactoperoxidase. Evidence for the Presence of a Low-Potential Compound II During Catalytic Turnover. *Biochemistry*. 1997 36, 1918-1926.

32. Lardinois, O.M., Medzihradszky, K.F., and Ortiz de Montellano, P.R. Spin Trapping and Protein Cross-linking of the Lactoperoxidase Protein Radical. *J. Biol. Chem.* 1999, 274, 35441-35448.

33. Filizola, M. and Loew, G. Role of Protein Environment in Horseradish Peroxidase Compound Formation: Molecular Dynamics Simulations of Horseradish Peroxidase – HOOH Complex. *J. Amer. Chem. Soc.* 2000, 122, 18-25.

34. Galijasevic, S., Saed, G.M., Diamond, M.P., and Abu-Soud, H.M. High Dissociation Rate Constant of Ferrous-dioxy Complex linked to the Catalase-Like Activity in Lactoperoxidase. *J. Biol. Chem.* 2004, 279, 39465-39470.

35. Abu-Soud, H.M.and Hazen, S. Interrogation of Mammalian Peroxidases with Diatomic Ligands. *Biochemistry.* 2001, 40, 10747-10755.

36. Gensch, T. and Viappiani, C. Time-Resolved Photothermal Methods: Accessing Time-Resolved Thermoynamics of Photoinduced Processes in Chemistry and Biology. *Photochem. Photobiol. Sci.* 2003, 2, 699-721.

37. Bialkowski, S.E. Photothermal Spectroscopic Methods for Chemical Analysis. *Chemical Analysis: A Series of Monographs on Analytical Chemistry and Its Applications.* Winefordner, J.D.; John Wiley & Sons: 1996; 134.

38. Hoyosa, T., Sakurada, J., Kurokawa, C., Toyoda, R., Nakamura, S. Interaction of Aromatic Donor Molecules with Lactoperoxidase Probed by Optical Difference Spectra. *Biochemistry.* 1989, 28, 2639-2644.

39. Miksovska, J., Norstrom, J., and Larsen, R. W. Thermodynamic Profiles for CO Photodissociation from Heme Model Compounds: Effect of Proximal Ligands. *Inorg. Chem.* 2005, 44, 1006-1014.

40. Martinez-Junza, V., Rizzi, A., Jolliffe, K. A., Head, N. J., Paddon-Row, M. N., Braslavsky, S. E. Conformational and Photophysical Studies on Porphyrin-containing Donor-bridge-acceptor Compounds. Charge Separation in Micellar Nanoreactors. Phys. Chem. Chem Phys. 2005, 7, 4114-4125.

41. Lange, R., Heiber-Langer, I., Bonfils, C., Fabre, I., Negishi, M., and Balny C. Activation Volumes and Energetic Properties of Binding of CO to Heme Proteins. *Biophys. J.* 1994, 66, 89-98.

42. Ohlsson, P.I., Blanck, J., Ruckpaul, K. Redution of Lactoperoxidase by the Dithionite Anion Monomer. Eur. J. Biochem. 1986, 158, 451-454.

43. Ohlsson, P-I. Lactoperoxidase, a Dithionite Ion Dismutase. *Eur. J. Biochem.* 1984, 142, 233-238.

44. Miksovska, J., Day, J., and Larsen, R.W. Volume and Enthalpy Profiles of CO Rebinding to Horse Heart Myoglobin. *J. Biol. Inorg. Chem.* 2003, 8, 621-625.

45. Arata, H., and Parson, W. Enthalpy and Volume Changes Accompanying Electron Transfer From P-870 to Quinones in Rhodopseudomonas Sphaeroides Reaction Centers. *Biochim. Biophys.* 1981, 636, 70-81.

46. Westrick, J. A., Peters, K. S., Ropp, J. D., and Sligar, S. G. Role of Arginin-45 Salt Bridge in Ligand Dissociation from Sperm Whale Carboxymyoglobin as Probed by Photoacoustic Calorimetry. *Biochemistry*. 1990, 29, 6741-6746.

47. Feis, A. and Angeloni, L. Photodissociation of the CO Complex of Horseradish Peroxidase Studied by Laser-Induced Optoacoustic Spectroscopy. *J. Phys. Chem. B.* 2001, 105, 2638-2643.